

Radio Interferometric Studies of Cool Evolved Stellar Outflows

A dissertation submitted to the University of Dublin
for the degree of Doctor of Philosophy

Eamon O’Gorman

Supervisor: Dr. Graham M. Harper

Trinity College Dublin, September 2013

SCHOOL OF PHYSICS
UNIVERSITY OF DUBLIN
TRINITY COLLEGE



Declaration

I declare that this thesis has not been submitted as an exercise for a degree at this or any other university and it is entirely my own work.

I agree to deposit this thesis in the University's open access institutional repository or allow the library to do so on my behalf, subject to Irish Copyright Legislation and Trinity College Library conditions of use and acknowledgement.

Name: Your Name

Signature: **Date:**

Summary

You should write a nice summary here...

A dedication if you wish...

Acknowledgements

Some sincere acknowledgements...

List of Publications

Refereed

1. **O’Gorman, E.**, Harper, G. M., Brown, J. M., Brown, A., Redfield, S., Richter, M. J., and Requena-Torres, M. A.
“CARMA CO(J = 2 - 1) Observations of the Circumstellar Envelope of Betelgeuse”
The Astronomical Journal, 144, 36 (2012)
2. Sada, P. V., Deming, D., Jennings, D. E., Jackson, B. K., Hamilton, C. M., Fraine, J., Peterson, S. W., Haase, F., Bays, K., Lunsford, A., and **O’Gorman, E.**
“Extrasolar Planet Transits Observed at Kitt Peak National Observatory”
Publications of the Astronomical Society of the Pacific, 124, 212 (2012)
3. Sada, P. V., Deming, D., Jackson, B. K., Jennings, D. E., Peterson, S. W., Haase, F., Bays, K., **O’Gorman, E.**, and Lundsford, A.
“Recent Transits of the Super-Earth Exoplanet GJ 1214b”
The Astrophysical Journal Letters, 720, L215 (2010)

Non-Refereed

1. **O’Gorman, E.**, & Harper, G. M.
“What is Heating Arcturus’ Wind?”,
Proceedings of the 16th Cambridge Workshop on Cool Stars, Stellar Systems and the Sun. Astronomical Society of the Pacific Conference Series, 448, 691 (2011)

Contents

List of Publications	vi
List of Figures	ix
List of Tables	x
1 Introduction	1
1.1 First Section	1
1.2 Second Section	1
1.3 Second Section	2
2 Introduction to Radio Interferometry	3
2.1 Radio Antenna Fundamentals	3
2.1.1 Properties of a Radio Antenna	4
2.1.2 Antenna Structural Design	7
2.1.3 Antenna Performance Parameters	9
2.2 Receiving System for an Interferometer	11
2.3 Fundamentals of Radio Interferometry	13
2.3.1 Young’s Slits	13
2.3.2 The Two-element Interferometer	15
2.3.3 Complex Visibility	19
2.3.4 Coordinate Systems for Imaging	20
2.4 Synthesis Imaging	21
2.4.1 Visibility Sampling	21
2.4.2 Imaging (Making a Dirty Map)	22
2.4.3 Deconvolution (Making a CLEAN map)	25

3	Targets, Instrumentation, and Observations	28
3.1	Betelgeuse	28
3.2	CARMA	28
3.3	CARMA Observations of Betelgeuse	28
3.4	Arcturus and Aldebaran	31
3.5	The Karl G. Jansky Very Large Array	35
3.6	VLA Observations of Arcturus and Aldebaran	39
A	A Nice Appendix	45
	References	46

List of Figures

1.1	Red Giant and Asymptotic Giant Branch Stars	2
2.1	Radiation and power pattern of a uniformly illuminated antenna.	6
2.2	Common optical systems used for radio antennas.	9
2.3	Block diagram of a superheterodyne receiver.	12
2.4	Fringe pattern produced by Young's slits under various situations.	14
2.5	Visibilities for various source sizes.	16
2.6	Simplified schematic diagram of a two-element interferometer.	17
2.7	The instantaneous point source responses of an interferometer.	18
2.8	The (u, v, w) interferometric coordinate system.	22
2.9	VLA antenna layout and two examples of $u - v$ coverage for different track lengths.	23
2.10	The Fourier transform pairs in synthesis imaging.	24
3.1	Main features of a VLA antenna.	38
3.2	Importance of offsetting source from phase center.	42
3.3	Overview of a low and high frequency VLA observation.	44

List of Tables

3.1	Physical Properties of α Ori.	29
3.2	CARMA Observations of α Ori.	30
3.3	Basic Properties of α Boo and α Tau.	33
3.4	Improved Performance Parameters of the VLA.	36
3.5	Frequency coverage, primary beam, and angular resolution of the VLA.	37
3.6	VLA Observations of α Boo and α Tau.	40

1

Introduction

Here is the introduction of the thesis, complete with a few references (Prothero & Buell, 2007; Sagan, 1997). Section 1.1 contains Equation 1.1, Section 1.2 has Figure 1.1 and Section 2.3 has Table 3.6. Chapter 2 has pretty much nothing in it.

1.1 First Section

This section has an equation. Here it is:

$$L_{\odot} = 4\pi R_{\odot}^2 \sigma T_e^4 \tag{1.1}$$

which is a nice way of describing the luminosity.

1.2 Second Section

So this section has a figure in it¹. That figure depicts the basic structure of a red giant.

¹And also a footnote.

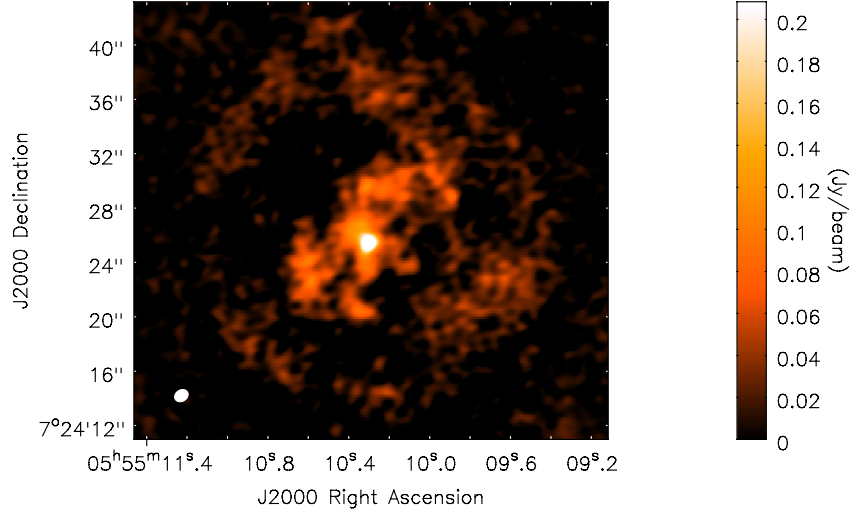


Figure 1.1: Red Giant and Asymptotic Giant Branch Stars. The left side of the figure shows the basic structure of a star on the giant branch of the HR diagram, while the right side shows a similar star after it has evolved to ascend the asymptotic giant branch. *Image Credit: Australian Telescope National Facility.*

1.3 Second Section

2

Introduction to Radio Interferometry

The poor spatial resolution provided by a single dish radio antenna can cause difficulties in obtaining accurate flux density measurements of radio astronomical sources, especially at long wavelengths. A single dish radio antenna is unable to distinguish against background radio emitters located in the primary beam, and therefore the observed flux density can contain emission from unrelated sources. This limitation can be overcome through interferometry. An interferometer acts as a spatial filter, and can discriminate against smooth backgrounds, while its higher resolution allows separation of the target from nearby confusing sources. This chapter describes the basic elements of a radio interferometer, what happens to the radio signal before it is sent for correlation, introduces the general concept of interferometry, and explains the process of synthesis imaging.

2.1 Radio Antenna Fundamentals

The quality and properties of the final radio image produced from a synthesis array are partially dependent on the properties of the individual antennas in the array. The most important such properties are discussed in the following sections and include aperture size, aperture efficiency, pointing accuracy and sidelobe

level. We define the radio antenna as the piece of equipment which converts the electromagnetic waves emitted from the observed source into an electric current ready to be input into the first low noise amplifier where the signal is at the radio/sky frequency, ν_{RF} . What happens to the signal after this will be discussed in Section 2.2.

2.1.1 Properties of a Radio Antenna

The power gain of a transmitting antenna is a measure of the antenna's capability of converting power into radio waves in a specific direction. In radio astronomy, the receiving counterpart of transmitting power gain is the effective collecting area of an antenna, $A(\nu, \theta, \phi)$, where ν is frequency and θ and ϕ are direction coordinates. An ideal radio antenna would collect all incident radiation from a distant point source and convert it to electrical power. The total spectral power P_ν collected by it would then be a product of its geometric area and the incident spectral power per area, or flux density F_ν . By analogy then, the effective area of a real radio antenna is defined

$$A(\nu, \theta, \phi) = \frac{P_\nu}{F_\nu} = \frac{P}{I(\nu, \theta, \phi) \Delta\nu \Delta\Omega} \quad (2.1)$$

where $I(\nu, \theta, \phi)$ is the source brightness in units $\text{W m}^{-2} \text{Hz}^{-1} \text{sr}^{-1}$ that the antenna is pointing at and P is the power (in Watts) received by the antenna in bandwidth $\Delta\nu$ from element $\Delta\Omega$ of solid angle. The normalized antenna reception pattern \mathcal{A} , often referred to as the power pattern due to the duality between receiving and transmitting, is defined as

$$\mathcal{A}(\nu, \theta, \phi) = \frac{A(\nu, \theta, \phi)}{A_0} \quad (2.2)$$

where A_0 (m^2) is often referred to as the effective area of the antenna and is the response at the center of the main lobe of $A(\nu, \theta, \phi)$ [i.e., $A(\nu, 0, 0)$]. Then the beam solid angle, Ω_A , of the primary beam is

$$\Omega_A = \iint_{\text{all sky}} \mathcal{A}(\theta, \phi) d\Omega \quad (2.3)$$

and is a measure of the field of view of the antenna.

2.1 Radio Antenna Fundamentals

In the case of an isotropic antenna [i.e., $\mathcal{A}(\nu, \theta, \phi) = 1$], it can be shown that the product of the effective area and the primary beam solid angle is equal to the square of the wavelength (Kraus *et al.*, 1986)

$$A_0 \Omega_A = \lambda^2. \quad (2.4)$$

Ω_A has its maximum possible value of 4π if \mathcal{A} is everywhere equal to 1. This means that the primary antenna can see the whole sky with equal sensitivity. Even though a large field of view is usually desirable in radio astronomy, Equation 2.4 ensures that for any given wavelength, when Ω_A is a maximum, the power received is a minimum and therefore the sensitivity is also at a minimum. To improve sensitivity, one could increase the collecting area of the antenna, but Equation 2.4 then ensures that the field of view must decrease. Thus, when deciding on the primary antenna size in a synthesis array, there is always a trade-off between field of view and sensitivity.

In reality, an antenna cannot radiate isotropically and will radiate preferentially in one or more directions. A Fourier transform relationship exists between the complex voltage distribution of the field, $f(u, v)$, in the aperture of the antenna and the complex far-field voltage radiation pattern, $F(l, m)$, of the antenna (Kraus *et al.*, 1986)

$$F(l, m) = \iint_{\text{aperture}} f(u, v) e^{2\pi i(ul+vm)} du dv \quad (2.5)$$

and

$$f(u, v) = \int_{-\infty}^{\infty} \int_{-\infty}^{\infty} F(l, m) e^{-2\pi i(ul+vm)} dl dm \quad (2.6)$$

where

$$u = \sin\theta\cos\phi \quad \text{and} \quad v = \sin\theta\sin\phi \quad (2.7)$$

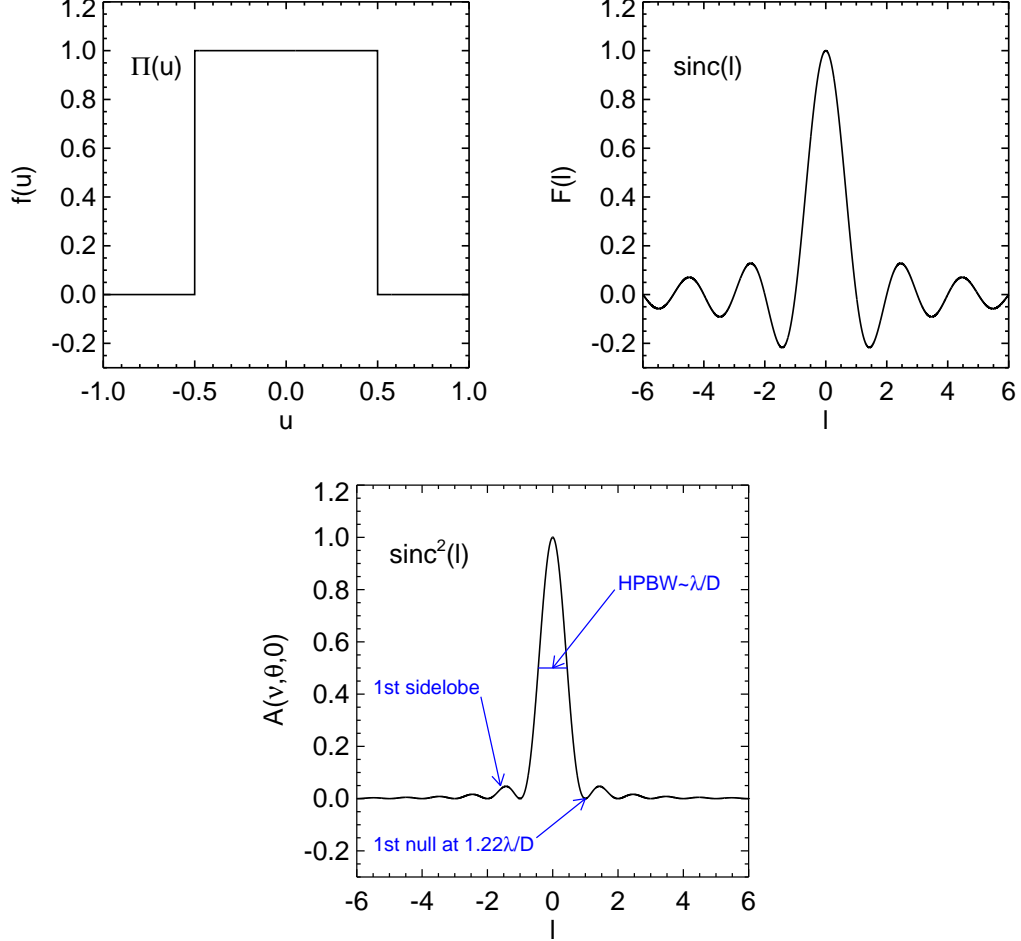


Figure 2.1: *Top Left:* A uniformly illuminated 1-D aperture $f(u)$. *Top Right:* The Fourier transform of $f(u)$ gives the antenna radiation pattern in the far-field, $F(l)$. *Bottom:* The power pattern of the antenna is given by $\mathcal{A} = |F(l)|^2$.

are the antenna coordinates and l and m are their Fourier counterparts. The form of $f(u, v)$ is determined by the manner in which the antenna feed illuminates the aperture. Therefore Equations 2.6 and 2.7 tell us that the radiation pattern in the far-field of a two-dimensional aperture is the two-dimensional Fourier transform of the aperture field illumination. For a uniformly illuminated 1-D aperture shown in Figure 2.1, the radiation pattern in the far-field is the *sinc* function. The radiation pattern in the far-field, $F(l, m)$, of such an antenna is related to the antenna power pattern by $\mathcal{A} = |F(l, m)|^2$. This power pattern is known as the Airy pattern if the antenna is uniformly illuminated and is also shown in Figure

2.1. The central peak of this power pattern is called the main beam while the smaller secondary peaks are called sidelobes. The antenna is maximally sensitive to radiation from the direction of the peak of the beam, but is also slightly sensitive to radiation in the direction of the side lobes. The half-power beamwidth (HPBW) of the main beam θ_{HPBW} is a term commonly used in the literature to describe the field of view of an antenna/interferometer and satisfies

$$\theta_{\text{HPBW}} \propto \frac{\lambda}{D} \quad (2.8)$$

where D is the diameter of the antenna. The constant of proportionality varies slightly with the illumination taper and can be shown to be equal to ~ 0.89 for a uniformly illuminated 1-D aperture and ~ 1.2 for most single dish radio antennas. When the sky is scanned with a single dish antenna, then this HPBW is the resolution of the resulting map.

2.1.2 Antenna Structural Design

The design of the primary antenna element of an interferometric array will depend on the wavelength range to be observed. In general, dipoles are used for wavelengths longer than ~ 1 m, while reflector antennas are typically used at shorter wavelengths. The reason why the more simple and less expensive dipoles are not used at all wavelengths is given by Equation 2.4. For an isotropic antenna, this equation tells us that the effective area is just

$$A_0 = \frac{\lambda^2}{4\pi}. \quad (2.9)$$

Therefore, at short wavelengths a non-directional antenna such as a dipole, will have a small effective collecting area, giving it poor sensitivity for reception. Thus, dipoles can be used at long wavelengths as they have sufficient collecting area, but cannot be used at shorter wavelengths as an impractical amount would be needed to produce useful collecting areas. Since the interferometric arrays used in this thesis use reflector antennas, the rest of this section will focus on them.

2.1 Radio Antenna Fundamentals

Choice of Antenna Mount. Nearly all interferometric arrays consist of antennas which have altitude over azimuth (alt-azimuth) mounts. These antennas lie on a horizontal azimuth track on which the antenna can turn in azimuth, and on a horizontal elevation axle about which the antenna can change in zenith angle. The main advantage of such a design is simplicity and thus lower cost. Gravity always acts on the reflector in the same plan thus reducing the problem of keeping the reflector profile accurate during the duration an observation. However, sources close to the zenith can usually not be observed due to the high rate of azimuth rotation required. Also, the beam rotates with respect to the source for long duration observations which can affect the dynamic range of total intensity images of very large sources. The other type of mount occasionally used is the equatorial mount. Its polar axis is aligned parallel to the axis of rotation of the Earth and therefore only needs to rotate about the declination axis to observe a source. Its beam also doesn't have the beam rotation problem encountered by the alt-azimuth design and can track sources close to the zenith. Its major disadvantage and the reason for its scarce usage is the complexity of its design and resulting increased cost.

Choice of Antenna Optics. In Figure 2.2 we show the main optical systems which can be used to feed a large radio reflector. The prime focus system (e.g. used in the Giant Meter Radio Telescope) has the advantage that it can be used at long wavelengths where the use of secondary focus feeds (i.e., sub-reflectors) become impractical. However, access to and space for the feeds and receivers are limited, and sensitivity can be lost due to spillover noise from the ground. The other designs have the advantage of easier access to the feeds and receivers and less spillover noise from the ground. The off-axis Cassegrain (e.g. used in the Very Large Array) also has the advantage of increased frequency capability as many feeds can be located in a circle around the center of the reflector and a slight rotation of the sub-reflector is all that is required to change observing frequency. The receivers and feeds in the Naysmith geometry (e.g. used in the Combined Array for Research in Millimeter wave Astronomy) are located externally to the antenna structure. Finally, the offset Cassegrain (e.g. used in the Green Bank Telescope)

has no blockage and will have a circularly symmetric beam with low sidelobes although the increase complexity of its structure leads to increased costs.

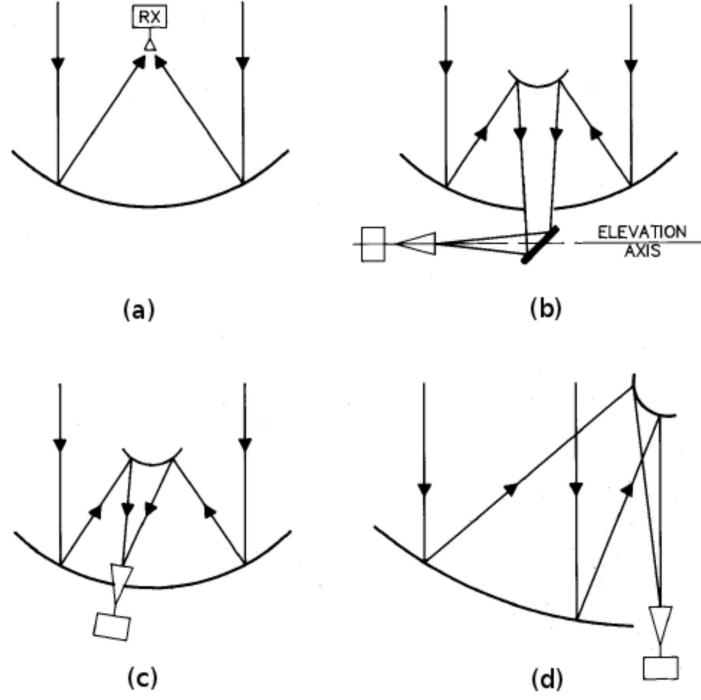


Figure 2.2: Common optical systems used for radio antennas. (a) Prime focus, (b) Naysmith, (c) Off-axis Cassegrain, (d) Offset Cassegrain [Figure adapted from Taylor *et al.* (1999)].

2.1.3 Antenna Performance Parameters

Aperture Efficiency. The geometric collecting area of a parabolic antenna A_{geo} ($= \pi D^2/4$) is related to the effective area (i.e., the collecting area when pointing directly at a source) via the dimensionless quantity η ($\eta < 1$) known as the aperture efficiency where

$$\eta = \frac{A_0}{A_{\text{geo}}}. \quad (2.10)$$

The aperture efficiency directly impacts on the sensitivity of the interferometric array and can be defined as the product of a number of different efficiency loss

2.1 Radio Antenna Fundamentals

factors,

$$\eta = \eta_{\text{sf}}\eta_{\text{bl}}\eta_{\text{s}}\eta_{\text{t}}\eta_{\text{misc}}. \quad (2.11)$$

The surface efficiency η_{sf} accounts for the aperture efficiency loss as a result of reflector profile inaccuracies. Such inaccuracies result in the electric field from various parts of the aperture not adding together in phase at the feed leading to a decrease in power. The aperture blockage efficiency η_{bl} accounts for the fact that the sub-reflector (or feed) and its support structure result in a reduction in the incident radiation on the antenna. The feed spillover efficiency η_{bl} is best understood if the antenna is considered in transmission rather than in reception mode, and is defined as the fraction of power radiated by the feed that is intercepted by the reflector for a prime focus system, or by the sub-reflector for a Cassegrain system. The illumination taper efficiency η_{t} accounts for the fact that the feed pattern does not illuminate the primary reflector uniformly but illuminates the outer part of the reflector at a lower level than the inner part. Finally, the miscellaneous efficiency losses such as reflector diffraction and feed position phase errors are accounted for in η_{misc} . As an example, the total aperture efficiency of the VLA antennas can vary between 0.65 and 0.2 at 6 and 0.7 cm, respectively.

Pointing Accuracy. The main lobe of an antenna's power pattern will usually not point exactly in the desired direction due to gravity deformations, wind pressure deformations, and mechanical inaccuracy. The angular offset, $\Delta\theta$, between the actual and desired pointing direction is called the pointing error. Usually, the desirable pointing error of an antenna at the highest operational frequency is $\Delta\theta < \theta_{\text{HPBW}}/20$ (Taylor *et al.*, 1999). With this specification reached, an antenna pointing at a compact source will suffer negligible intensity variations as $\mathcal{A}(\theta_{\text{HPBW}}/20) > 0.99$. However, this pointing error of only $\theta_{\text{HPBW}}/20$ will still have a substantial effect on the accuracy of the outer image. For example, a source located at the half power point will suffer a substantial fractional intensity variation of $2\mathcal{A}(\theta_{\text{HPBW}}/2 + \theta_{\text{HPBW}}/20) \simeq 0.86$. The blind pointing of a VLA antenna is only about $10''$ and can be much worse in daytime, occasionally exceeding $1'$. This means that at Q-band (45 GHz; 0.7 cm), which is the highest observing frequency on the VLA, the pointing error is only at best $\theta_{\text{HPBW}}/6$, and

at worst $> \theta_{\text{HPBW}}$, meaning that the target may lie outside of the primary beam. To overcome this problem of large antenna pointing errors at high frequencies with the VLA, a technique known as referenced pointing is implemented. This technique will be discussed further in Chapter 3.

2.2 Receiving System for an Interferometer

A radiometer (a radio receiver) is a device used to measure the timed-averaged power of the noise coming from a radio telescope within a well-defined radio frequency (RF) range, $\nu_{\text{RF}} - \Delta\nu_{\text{RF}}/2 \rightarrow \nu_{\text{RF}} + \Delta\nu_{\text{RF}}/2$, where $\Delta\nu_{\text{RF}}$ is the bandwidth of the receiver and $\Delta\nu_{\text{RF}} < \nu_{\text{RF}}$. The simplest radiometer carries out the following tasks:

1. Filters the broadband noise coming from the antenna via a bandpass filter.
2. Multiplies the filtered voltage by itself (i.e., its output voltage is proportional to its input power).
3. Smooths out the rapidly fluctuating output of the detected voltage via a signal averager or integrator.
4. Measures the smoothed voltage.

In practice, radiometers are never as simple as those described above and nearly all practical radiometers are *superheterodyne* receivers which incorporate a number of additional steps to produce an output voltage.

The RF front end is the term used to describe all the circuitry between the feed horn and the lower intermediate frequency (IF) stage. The first task of the front end is to amplify the received signal. The radio signals we want to measure are generally very weak and therefore need to be initially amplified by many orders of magnitude so they are above the noise level in succeeding stages. However, the front end electronic components produce random electrical noise which will also get amplified by this large amount. Therefore the role of the pre-amplifier is to amplify the incoming signal from the antenna while adding as little noise as possible. For this reason, the pre-amplifier is often called a low noise amplifier

2.2 Receiving System for an Interferometer

(LNA) and are often cooled to very low temperatures to minimize the amount of noise contributed by the components.

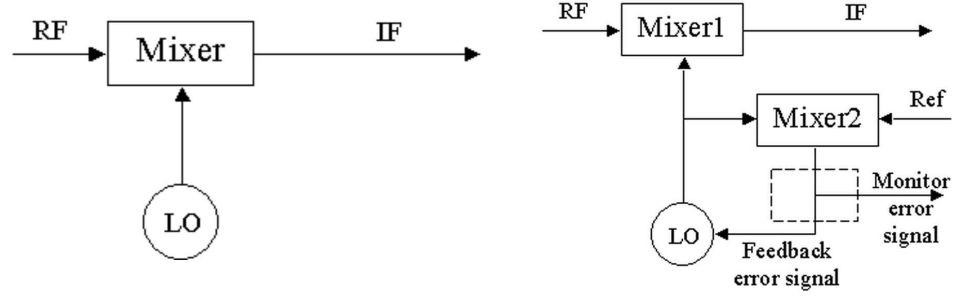


Figure 2.3: *Left:* Block diagram of a simple superheterodyne receiver. The amplified RF signal is mixed with a signal from a local oscillator to convert the signal to the more manageable intermediate frequency. *Right:* For interferometry, a phase lock loop is used to ensure all antennas are locked to the same frequency.

The amplified RF signal is then sent through a mixer which multiplies the RF signal by a sine wave of frequency ν_{LO} which is generated by a local oscillator (LO), as shown in Figure 2.3. The effect of this is that RF signal is changed to a lower frequency which can be easier handled by the IF amplifier and improves frequency selectivity. Mathematically, the mixer does the following

$$2\sin(2\pi\nu_{LO}t) \times \sin(2\pi\nu_{RF}t) = \cos[2\pi(\nu_{LO} - \nu_{RF})t] - \cos[2\pi(\nu_{LO} + \nu_{RF})t], \quad (2.12)$$

and produces two additional outputs, one at the input signal frequency minus the local oscillator frequency, and one at the sum of these frequencies. The lower of the two outputs called the intermediate frequency (IF) is taken by passing the mixer output through a filter in the IF amplifier. In interferometry, where the signals from two antennas are correlated, it is crucial that the receivers from both antennas are operating at the same frequency to control the phase difference between them. This is achieved by using a phase lock system, whose block diagram is laid out in Figure 2.3. In this system another mixer compares the LO to a reference frequency, which is the same for all antennas. Any existing phase error results in an error signal that is sent back to the oscillator so that its frequency can be adjusted to maintain exact frequency tuning. After this, the IF can finally be sent to the radiometer and recorded.

2.3 Fundamentals of Radio Interferometry

The angular resolution $\Delta\theta$ of a radio antenna is the minimum angular separation which two point sources can have in order to be recognized as separate objects. The *Rayleigh criterion* is the generally accepted criterion for defining the angular resolution of a filled circular aperture of diameter D , at the observational wavelength λ and is given as

$$\Delta\theta = 1.22 \frac{\lambda}{D} \text{ rad.} \quad (2.13)$$

The Rayleigh criterion states that two objects are resolved when the first null of the diffraction pattern of one object coincides with the maximum of the diffraction pattern of the other. An immediate consequence of Equation 2.13 is that at large wavelengths, the angular resolution becomes large unless the diameter of the aperture can be increased substantially. In order to achieve modest angular resolution at radio wavelengths with a single radio antenna then, the diameter becomes impractically large. For example, in order to achieve an angular resolution of $1''$ at 6 cm a 12 km aperture would be required. Radio interferometry is a technique used in radio astronomy to overcome this problem of poor angular resolution at long wavelengths.

2.3.1 Young's Slits

The basic principles of interferometry can be understood through Young's double-slit experiment. If coherent radiation emitted from a distant point source propagates through two slits, an illumination pattern composed of bright and dark fringes is observed. The phenomenon is a result of the constructive and destructive interference between the secondary waves produced by the slits. The fringe separation is λ/B , where B is the projected separation of the slits and is called the baseline. The fringe contrast which is historically known as the fringe visibility, V , can be written as

$$|V| = \frac{I_{\max} - I_{\min}}{I_{\max} + I_{\min}} \quad (2.14)$$

where I_{\max} and I_{\min} are the maximum and minimum intensity of the fringes, respectively. In other words, the fringe visibility is the fringe amplitude normalized

by the sum of the maximum and minimum intensity.

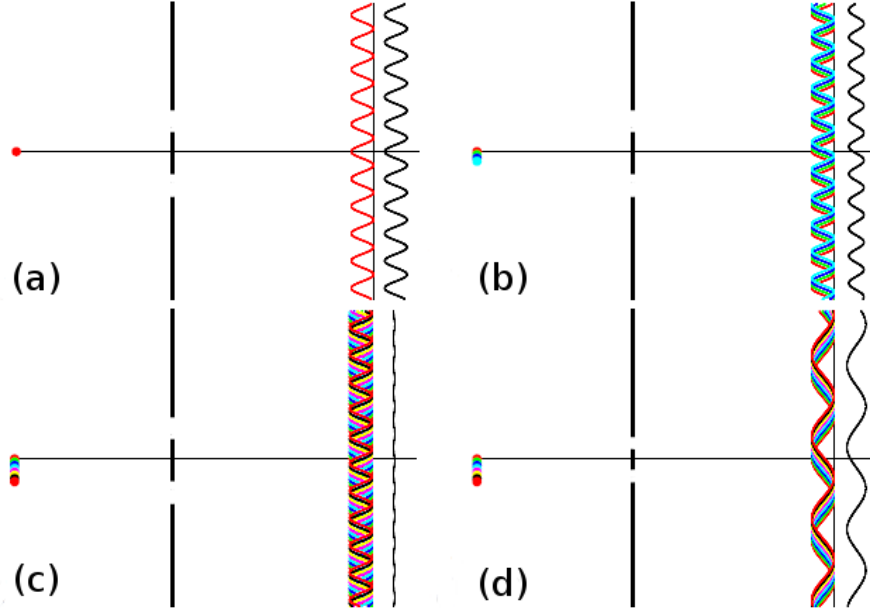


Figure 2.4: The resulting fringe pattern produced by Young’s slits under various conditions. The source is shown on the left of the slits in each panel, while the separate fringe patterns (colors) along with the added fringe pattern (black) is shown on the right of the slits. (a) Point source at infinity, (Visibility = 1). Fringes are separated by an angular distance of λ/B . (b) An increase in source size results in a drop in visibility. (c) When the source size is equal to λ/B , the visibility is zero. (d) If the source size remains the same as in (c) and the slit spacing is reduced, then the fringes re-appear. Figure adapted from [Jackson \(2008\)](#).

In the simple case shown in Figure 2.4a, the angular size of the source is $\ll \lambda/B$ and the fringe visibility is 1. In interferometry, this equates to the situation in which the source size is smaller than the synthesized beam and only an upper limit of the source size can be obtained (i.e., the source is unresolved). In Figure 2.4b, the angular size of the source is now larger and can be thought of as a sequence of point sources each emitting radiation which is uncorrelated with emission from the others. An angular shift of ϕ , called phase, in the sources position results in a shift in the corresponding fringe pattern by the same angle the other way. The total interference intensity pattern is then just the sum of these individual patterns and the visibility is reduced. When the extension of the

2.3 Fundamentals of Radio Interferometry

source equals λ/B , the fringes disappear and give a constant illumination pattern. In this case the fringe visibility is zero and the source is completely resolved as shown in Figure 2.4c. Finally, if the source size is the same as that in Figure 2.4c but the slit separation is reduced, then the fringe separation λ/B will again increase as shown in Figure 2.4d. This is because the source now produces much less displacement of the fringe patterns as a fraction of the fringe separation. In interferometry, this result means that extended sources can only be probed with short baselines.

Visibility and phase are often expressed together as the complex visibility $V = |V|e^{i\phi}$, which completely defines a pattern of interference fringes. Young's double-slit experiment demonstrates a fundamental property of interferometry, namely that the contrast of fringes is a function of the geometry of the source. The results of the experiment are summarized in Figure 2.5. The top row shows that a large source (i.e., one whose intensity distribution extends out to a large angle on the sky) has a fringe visibility pattern which falls off quickly as projected baseline length increases. The bottom row shows that for compact sources the fringe visibility remains high out to large baselines. In the following section we will show that the relationship between the sky brightness distribution $I(\theta)$ and the visibility $V(B)$ is a Fourier transform.

2.3.2 The Two-element Interferometer

Interferometers with N antennas can be treated as $N(N - 1)/2$ independent interferometer pairs so it is worthwhile studying the simplest case of the two-element interferometer. A simplified block diagram of the components of such an interferometer is shown in Figure 2.6. The figure shows two identical antennas separated by a baseline vector \mathbf{b} pointing towards a distant radio source in a direction indicated by the unit vector \mathbf{s} . The plane waves from the distant radio source reach antenna 1 at a time τ_g later than they reach antenna 2. τ_g is called the geometric delay and is given by

$$\tau_g = \frac{\mathbf{b} \cdot \mathbf{s}}{c} = \frac{b \cos \theta}{c} \quad (2.15)$$

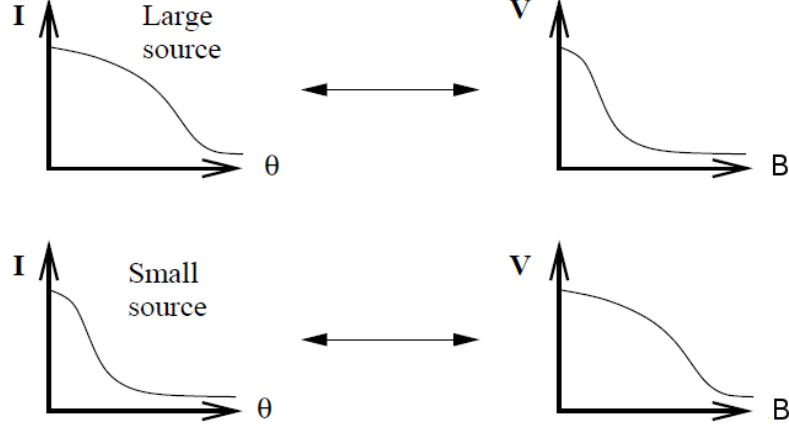


Figure 2.5: *Left column:* Intensity distribution as a function of sky angle for an extended source (top) and for a more compact source (bottom). *Right column:* The corresponding fringe visibility as a function of slit separation or baseline. Figure adapted from [Jackson \(2008\)](#).

where c is the speed of light. If we assume that the interferometer only responds to a very narrow band centered on frequency $\nu = \omega/2\pi$, then the output voltages of antennas 1 and 2 at time t can be written as

$$V_1(t) = V \cos[\omega(t - \tau_g)] \quad \text{and} \quad V_2(t) = V \cos(\omega t). \quad (2.16)$$

The signals are then passed through a correlator which first multiplies these voltages to give

$$V_1(t)V_2(t) = \frac{V^2}{2} [\cos(2\omega t - \omega\tau_g) + \cos(\omega\tau_g)] \quad (2.17)$$

and then averages them over a time interval Δt which is long enough such that $\Delta t \gg (2\omega)^{-1}$ to give the final output R :

$$R = \langle V_1(t)V_2(t) \rangle = \frac{V^2}{2} [\cos(\omega\tau_g)]. \quad (2.18)$$

As the Earth rotates, τ_g varies slowly with time and the resultant oscillations in the correlator output voltage represent the motion of the source. These

2.3 Fundamentals of Radio Interferometry

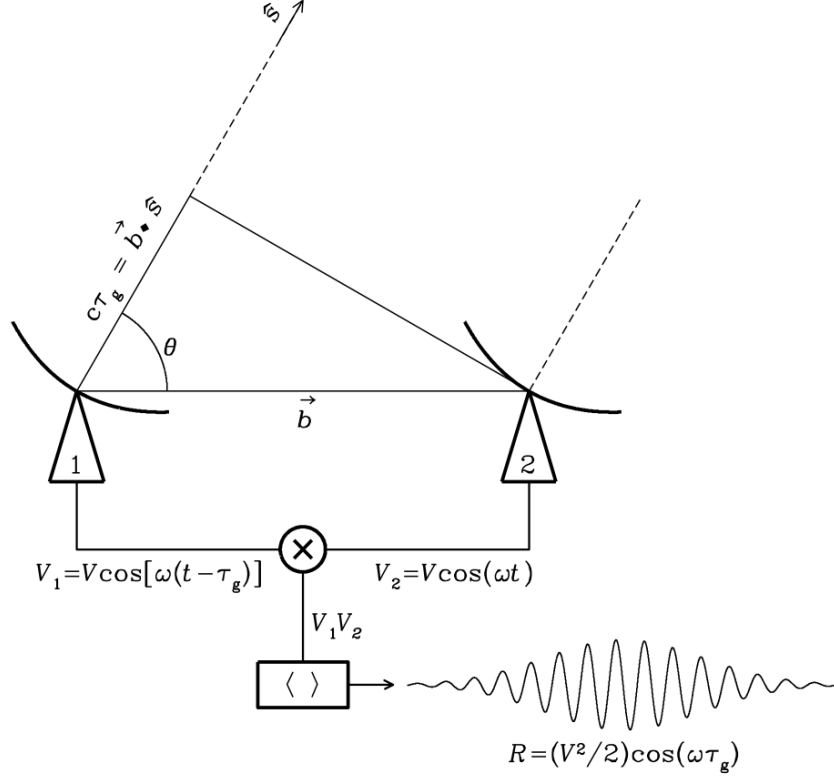


Figure 2.6: Simplified schematic diagram of a two-element interferometer. The correlator multiplies and averages the voltage outputs V_1 and V_2 of the two dishes and yields an output amplitude $V^2/2$ which is proportional to the point-source flux density F_ν . *Image Credit:* National Radio Astronomy Observatory.

sinusoidal oscillations are called fringes, and the fringe phase is

$$\phi = \omega \tau_g = \frac{\omega b \cos \theta}{c} \quad (2.19)$$

which changes with source direction as follows

$$\frac{d\phi}{d\theta} = \frac{\omega b \sin \theta}{c} = 2\pi \left(\frac{b \sin \theta}{\lambda} \right). \quad (2.20)$$

The fringe phase completes a full period (i.e., $\Delta\phi = 2\pi$) when an angular change $\Delta\theta = (\lambda/b \sin \theta)$ occurs. This tells us that the fringe phase is an extremely sensitive measure of source position if the projected baseline $b \sin \theta$ is many wavelengths long

2.3 Fundamentals of Radio Interferometry

and is the reason why interferometers can determine the positions of compact radio sources with exquisite accuracy.

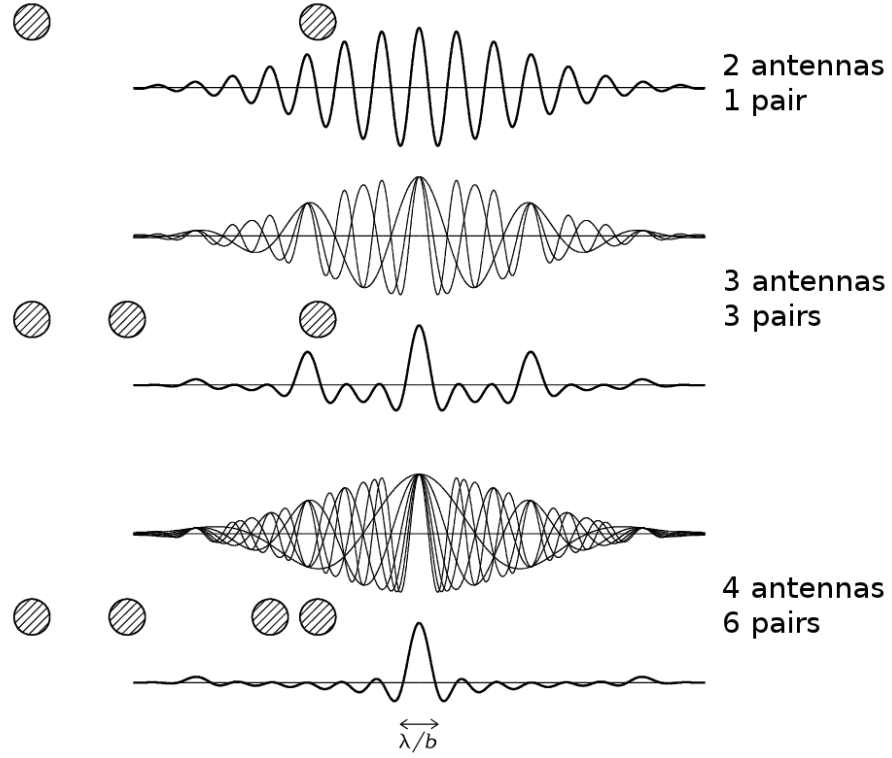


Figure 2.7: The instantaneous point source responses of an interferometer with two, three and four elements is indicated by the thick curves. The individual responses of the three pairs of two-element interferometers of the three-element interferometer and the six pairs of two-element interferometers of the four-element interferometer are plotted as thin curves. The main beam of the four-element interferometer is nearly Gaussian and has a width of $\sim \lambda/B$. This is known as the instantaneous synthesized beam of the interferometer. *Image Credit:* National Radio Astronomy Observatory.

If the antennas in an interferometric array are isotropic, then the point-source response of the interferometer would be a sinusoid spanning the entire sky and the interferometer would be only sensitive to one Fourier component of the sky brightness distribution having angular period $\lambda/b\sin\theta$. The response of a two-element interferometer R with non-isotropic antennas is this sinusoid multiplied by the product of the voltage patterns (i.e., defined as $f(u, v)$ in Section 2.1.1)

2.3 Fundamentals of Radio Interferometry

of the individual antennas. If the antennas are identical then this product is the power pattern of the individual antennas called the primary beam. The primary beam is usually a Gaussian that is much wider than the fringe period as $D \ll b \sin \theta$. The result is that an interferometer with directive antennas responds to a finite range of angular frequencies centered on $b \sin \theta / \lambda$. The instantaneous point source response of an interferometer is known as the synthesized beam and is the point source response obtained by averaging the outputs of all antenna pairs. The synthesized beam of an interferometer is an important quantity as it defines the maximum angular resolution of the instrument. The synthesized beams produced by an interferometer with a various number of antennas arranged in 1-D is shown in Figure 2.7. The figure shows that the synthesized beam can be improved by acquiring more Fourier components (i.e., baselines) and rapidly approaches a Gaussian as N increases. However, sidelobes are still significant and a broad negative “bowl” exists between the main beam and the first sidelobes due to the absence of short spacings.

2.3.3 Complex Visibility

The interferometer output can be expressed in terms of the radio brightness over the sky, which is sometimes also called specific intensity and has units $\text{W m}^{-2} \text{Hz}^{-1} \text{sr}^{-1}$. If the radio brightness of a spatially incoherent extended source in the direction of unit vector \mathbf{s} is $I(\mathbf{s})$, then the response of the two-element interferometer with “cosine” correlator output near frequency $\nu = \omega/2\pi$ is obtained by treating the extended source as the sum of independent point sources:

$$R_c = \int_{\Omega} \mathcal{A}(\mathbf{s}) I_{\nu}(\mathbf{s}) \cos \left(\frac{2\pi \mathbf{b} \cdot \mathbf{s}}{\lambda} \right) d\Omega \quad (2.21)$$

where \mathcal{A} is the normalized antenna reception pattern defined in Section 2.1.1 and we call $\mathcal{A}(\mathbf{s}) I_{\nu}(\mathbf{s})$ the modified brightness distribution. However, the cosine function in the “cosine” correlator output is only sensitive to the even part of the sky brightness distribution, which can be written as the sum of even and odd parts:

$$I(\mathbf{s}) = I_e(\mathbf{s}) + I_o(\mathbf{s}). \quad (2.22)$$

2.3 Fundamentals of Radio Interferometry

A “sine” correlator whose output is odd, is needed to detect the odd part of $I(\mathbf{s})$ and this is implemented by inserting a 90° phase delay into the signal of one of the antennas to give

$$R_s = \int_{\Omega} \mathcal{A}(\mathbf{s}) I_{\nu}(\mathbf{s}) \sin\left(\frac{2\pi \mathbf{b} \cdot \mathbf{s}}{\lambda}\right) d\Omega \quad (2.23)$$

It is convenient to write the cosines and sines as complex exponentials using the identity

$$e^{i\phi} = \cos(\phi) + i\sin(\phi) \quad (2.24)$$

and so the combination of “cosine” and “sine” correlators is called a “complex” correlator. The term *visibility* was first introduced by [Michelson \(1890\)](#) to describe the relative amplitudes of the optical fringes that he observed. The visibility is a complex quantity in radio astronomy and has dimensions of spectral power flux density ($\text{W m}^{-2} \text{Hz}^{-1}$). The complex visibility is the response of a two-element interferometer with a complex correlator to an extended source with brightness distribution $I(\mathbf{s})$ and is defined as

$$V \equiv R_c - iR_s, \quad (2.25)$$

i.e.,

$$V_{\nu} = \int_{\Omega} \mathcal{A}(\mathbf{s}) I_{\nu}(\mathbf{s}) e^{-2\pi i \nu \mathbf{b} \cdot \mathbf{s} / c} d\Omega. \quad (2.26)$$

2.3.4 Coordinate Systems for Imaging

The baseline vector \mathbf{b} has coordinates (u, v, w) in three dimensions shown in Figure 2.8 where w points in the directions of interest, i.e., towards a direction s_0 that becomes the center of the synthesized image. u , v and w are measured in wavelengths (i.e., the components of \mathbf{b}/λ) and have directions towards the East, the North and the phase tracking center, respectively. An arbitrary unit vector \mathbf{s} has components (l, m, n) called direction cosines, where $n = \cos\theta =$

$(1 - l^2 - m^2)^{1/2}$. Using these coordinates the parameters in Equation 2.26 become

$$\begin{aligned} \frac{\nu \mathbf{b} \cdot \mathbf{s}}{c} &= ul + vm + wn, \\ d\Omega &= \frac{dl dm}{n} = \frac{dl dm}{\sqrt{1 - l^2 - m^2}}. \end{aligned} \quad (2.27)$$

Therefore Equation 2.26 can be defined in terms of the coordinate system laid out in Figure 2.8 as

$$V_\nu(u, v, w) = \int_{-\infty}^{\infty} \int_{-\infty}^{\infty} \mathcal{A}_\nu(l, m) I_\nu(l, m) e^{-2\pi i [ul + vm + w(\sqrt{1 - l^2 - m^2})]} \frac{dl dm}{\sqrt{1 - l^2 - m^2}} \quad (2.28)$$

which is not a three-dimensional Fourier transform. This equation becomes a two-dimensional Fourier transform if $w = 0$ which is a good approximation for small field imaging, i.e., when $|l|$ and $|m|$ are small. In this case Equation 2.28 can be inverted to find the modified sky brightness distribution:

$$\mathcal{A}_\nu(l, m) I_\nu(l, m) = \int_{-\infty}^{\infty} \int_{-\infty}^{\infty} V_\nu(u, v) e^{2\pi i (ul + vm)} du dv. \quad (2.29)$$

Therefore Equation 2.29 demonstrates the important Fourier Transform relationship between the sky brightness distribution and the complex visibility (i.e., the interferometer response).

2.4 Synthesis Imaging

A synthesis imaging telescope consists of a number radio antennas fixed on the ground and uses the Earth's rotation to vary the projected baseline coverage to increase the sampling of the $u - v$ plane. In this section we describe how Earth-rotation aperture synthesis is used to convert the complex visibilities outputted from the correlator to a final radio image of the observed sky.

2.4.1 Visibility Sampling

An example of how a radio interferometer samples the $u - v$ plane is shown in Figure 2.9. The left panel of this figure shows the overhead view of the VLA in its

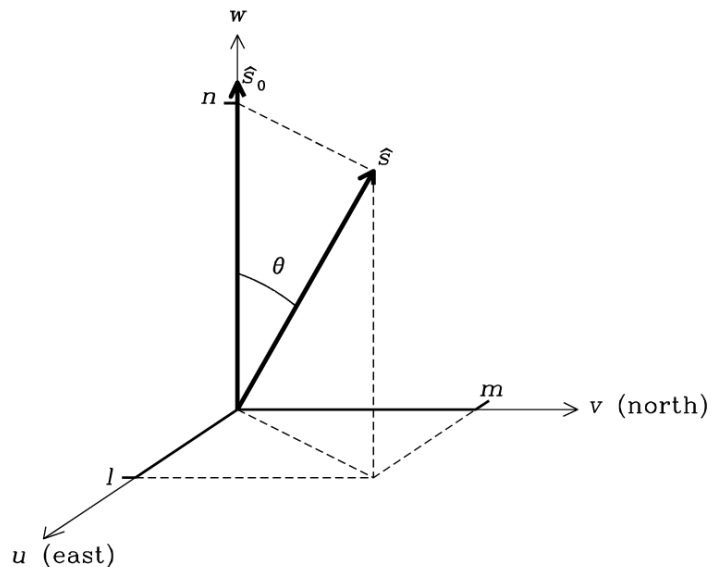


Figure 2.8: The (u, v, w) interferometric coordinate system. l , m , and n are the projections of the unit vector \mathbf{s} onto the u , v , and w axes, respectively.

most extended configuration while the other two panels shows the corresponding $u-v$ coverage for different periods of time. We define u and v as the east-west and north-south components of the projected baseline in wavelengths, respectively. As the Earth rotates, the projected baseline of every two-element pair in the array changes, thus sampling a different part of the $u-v$ plane. The middle panel shows that the total $u-v$ coverage of the VLA for a very short duration track (i.e., a snapshot) results in a ‘snowflake’ like pattern, with more dense coverage in the direction of the arms of the array due to the larger number of baselines. Most radio interferometers have their own unique array configuration layout and thus produce a different ‘snapshot’ $u-v$ coverage to that shown in Figure 2.9. Over many hours, the $u-v$ points trace out portions of ellipses and eventually after a full Earth rotation the points can trace out full ellipses as shown in the right panel of Figure 2.9.

2.4.2 Imaging (Making a Dirty Map)

For every sky brightness distribution $I(l, m)$ there exists a continuous complex visibility function $V(u, v)$ that is its Fourier Transform. An array of antennas

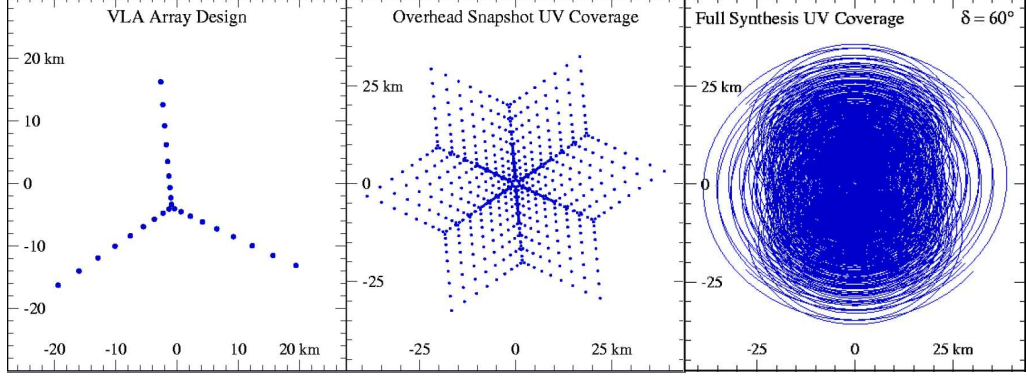


Figure 2.9: *Left:* The VLA in A-configuration is an example of an ‘Y’ shaped array design. *Middle:* The corresponding overhead snapshot $u-v$ coverage results in ‘snowflake’ pattern. *Right:* The corresponding $u-v$ coverage after a 12 hour track of a source at a declination of 60° . Note the more intense $u-v$ coverage in the direction of the three straight arms of the VLA for a snapshot track compared to the more uniform coverage over a longer duration track.

will only ever measure a certain set of values of this visibility function where the measured set is called the sampling function $S(u, v)$. This function is zero where no data have been taken. The actual data provided by the array is known as the sampled visibility function, $S(u, v)V(u, v)$. If we take the inverse Fourier transform of this function we get what is known as the *dirty image*:

$$I_\nu^D(l, m) = \int_{-\infty}^{\infty} \int_{-\infty}^{\infty} S(u, v) V_\nu(u, v) e^{2\pi i(ul+vm)} du dv. \quad (2.30)$$

where we have used $I_\nu(l, m)$ to denote the modified sky brightness $\mathcal{A}(l, m)I_\nu(l, m)$ as the correction for primary beam can be made at the final stage of data processing. Using the convolution theorem, the relationship between the dirty image and the desired intensity distribution $I_\nu(u, v)$ is

$$I_\nu^D(u, v) = I_\nu(u, v) * B(l, m) \quad (2.31)$$

where the asterisk implies convolution and

$$B(l, m) = \int_{-\infty}^{\infty} \int_{-\infty}^{\infty} S(u, v) e^{2\pi i(ul+vm)} du dv \quad (2.32)$$

is the *point spread function* (PSF), or *synthesized beam*, or *dirty beam* (i.e., the inverse Fourier Transform of the sampling function S). Equation 2.31 says that the dirty image I^D is the true intensity distribution I , convolved with the synthesized beam B .

In Figure 2.10 we graphically summarize what has been said above. The panels in the upper row show the sky plane representations of the true image, the point spread function and the dirty image, while the panels in the lower row show the corresponding $u-v$ plane representations of the true visibility, the sampling function and the sampled visibility. In other words, Equation 2.29 is summarized graphically by the relationship between panels (a) and (d), Equation 2.32 by (b) and (e), and Equations 2.30 and 2.31 by (c) and (f).

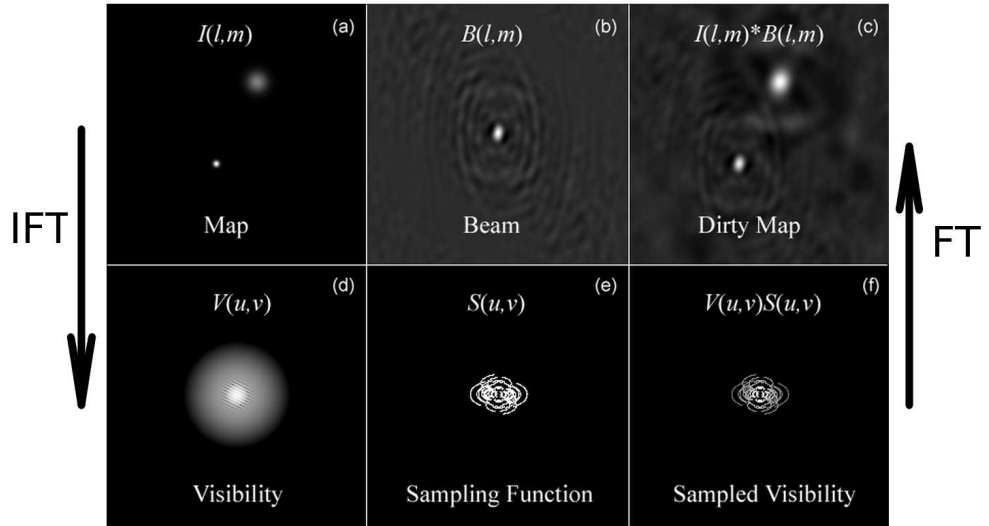


Figure 2.10: The Fourier transform pairs in synthesis imaging. (a) and (d): The true sky brightness and the visibility. (b) and (e): The dirty beam and the sampling function. (c) and (f): The dirty image and the sampled visibility. *Image Credit:* Prof. Dale E. Gary (New Jersey Institute of Technology).

Before the dirty image is computed, a weighting system is often applied to the visibilities to control the PSF. The two most common types of weighting system used are:

$$D_k = 1, \quad \text{natural weighting} \quad (2.33)$$

$$D_k = \frac{1}{N_s(k)}, \quad \text{uniform weighting} \quad (2.34)$$

where D_k is the weight to be applied to cell k , and $N_s(k)$ is the number of data samples falling into cell k of characteristic width s . Natural weighting treats all points alike and gives the best signal-to-noise ratio for detecting weak sources. However, it produces a beam with a broad low-level plateau which is undesirable when imaging sources with both large and small scale structure. Uniform gridding produces fewer artifacts in the final map, while keeping the full resolution of the array but gives poorer signal-to-noise than natural weighting.

The ‘direct Fourier transform’ method can then be used to solve for the dirty image Equation 2.30. However, if this method is evaluated at every point on a $N \times N$ grid, then the number of multiplications required goes as N^4 . The fast Fourier transform (FFT) algorithm can also be used to solve Equation 2.30 but requires interpolating the data onto a regular grid (i.e., a process known as *gridding*). This method is widely used for large data volumes as it requires only a few times $N^2 \log_2 N$ operations - not $\mathcal{O}(N^4)$, and the total time taken for gridding and FFT is usually a lot less than would take using the direct Fourier transform method.

2.4.3 Deconvolution (Making a CLEAN map)

The solution to the inverse Fourier transform given in Equation 2.29 is not unique, because the unmeasured points in the $u - v$ plane could have *any* value without violating the data constraints. The ‘principle solution’ is the one in which all missing $u - v$ measurements are set to zero and gives the dirty image discussed in the previous section. The dirty image is usually not a satisfactory representation of the sky as one would expect a more continuous distribution of visibilities than that provided by the array. The goal of the deconvolution process is to find a method that determines more reasonable values for the unmeasured $u - v$ data. A priori information is the key to choosing ‘reasonable’ values. For example, we know that the Stokes parameter I must be positive and that radio sources generally do not have sidelobe patterns.

The CLEAN algorithm (Högbom, 1974) is the most widely used technique in radio interferometry to deconvolve the true sky intensity from the dirty beam. It assumes that the radio source can be represented by a number of point sources in an otherwise empty field and a simple iterative process is used to find the strengths and positions of these point sources. The final CLEAN image (i.e., the deconvolved image) is the sum of these point sources convolved with a CLEAN beam, which is usually an elliptical Gaussian of the same size and shape as the inner part of the dirty beam. The CLEAN algorithm obeys the following steps:

1. Find the strength and position of the brightest point in the dirty image. It may also be desirable to search for peaks in specified areas of the image, called CLEAN windows or regions.
2. At this position in the dirty image, subtract the dirty beam multiplied by the peak strength and a damping factor g ($g \leq 1$, usually called the loop gain).
3. Record the position and the subtracted flux in a model.
4. Iterate between (1), (2), and (3) until the peak is below some user specified level. The remainder of the dirty image is now termed the residuals.
5. Convolve the accumulated point source model with an idealized CLEAN beam (usually an elliptical gaussian of the same size and shape as the central lobe of the dirty beam).
6. Add the residuals to the image in (5) to create the final CLEAN image.

A problem with CLEAN is that the final CLEANed image is somewhat dependent upon the various control parameters such as CLEAN boxes, the loop gain and the number of CLEAN subtractions. For example, using too high a gain tends to make extended, weak emission undetectable and noisy. This problem is unavoidable, and input values must be chosen on a case by case basis, depending on the source and data quality.

Another deconvolution algorithm used in radio synthesis imaging, albeit less often, is the Maximum Entropy Method (MEM) which operates by minimizing a

smoothness function (‘entropy’) in an image. To conclude this section, we briefly discuss the practical differences between CLEAN and MEM:

1. CLEAN is nearly always faster than MEM, unless the image contains more than 1 million pixels.
2. MEM images are nearly always smoother than CLEAN images. This is because for CLEAN, what happens at one pixel is not coupled to what happens to its neighbours, while MEM couples pixels together by minimizing the spread in pixel values.
3. CLEAN sometimes makes extended emission look blotchy and may introduce artificial stripes into the image while MEM copes very poorly with point sources in extended emission. (Multi-scale CLEAN which is discussed in Chapter 3 is now becoming a popular choice in the radio community as an alternative deconvolution algorithm for images containing extended emission.)
4. For MEM, it is necessary to know the noise level quite well and it also helps to know the total flux density of the image. Knowledge of these are not required for CLEAN.

3

Targets, Instrumentation, and Observations

3.1 Betelgeuse

decin proposal, paper intro, CO

3.2 CARMA

3.3 CARMA Observations of Betelgeuse

3 configurations, max and min resolutions, variability of phase cals, flux cals

3.3 CARMA Observations of Betelgeuse

Table 3.1: Physical Properties of α Ori.

Property	α Ori	Reference
HD Number	124897	
Spectral Type	K2 III	
ra (ICRS: ep=J2000)	14 ^h 15 ^m 39.672 ^s	
dec (ICRS: ep=J2000)	+19 10 56.673	
pm-ra (mas yr ⁻¹)	-1093.39 ± 0.44	
pm-dec (mas yr ⁻¹)	-2000.06 ± 0.39	
π (mas)	88.83 ± 0.54	
Distance (pc)	11.3±0.1	
M (M_{\odot})	0.8±0.2	
θ_{UD} (mas)	21.0±0.2	
θ_{LD} (mas)	21.0±0.2	
L (L_{\odot})		
R (R_{\odot})	25.4±0.3	
Log g		
T_{eff} (K)	4294±30	
v_{rad} (km s ⁻¹)	+5.19 ± 0.04	
v_{esc} (km s ⁻¹)	110	
v_{∞} (km s ⁻¹)	~40	
T_{wind} (K)	~10,000	
\dot{M} (M_{\odot} yr ⁻¹)		
H (H_{\odot})		
Fe/H	-0.5±0.2	

Table 3.2: CARMA Observations of α Ori between June 2007 and November 2009.

Date	Configuration	Time on Source (hr)	Flux Calibrator	Phase Calibrator	Image Cube Dynamic Range
2007 Jun 18	D	0.9	0530+135	0530+135, 0532+075	22.8
2007 Jun 21	D	3.0	0530+135	0530+135, 0532+075	22.7
2007 Jun 24	D	2.1	0530+135	0530+135, 0532+075	26.1
2007 Jun 25	D	2.4	0530+135	0530+135, 0532+075	30.2
2009 Jul 07	E	3.2	3C120	3C120, 0532+075	30.1
2009 Nov 05	C	1.2	3C120	3C120, 0532+075	17.3
2009 Nov 09	C	3.0	3C120	3C120, 0532+075	27.2
2009 Nov 15	C	1.0	3C120	3C120, 0532+075	17.8
2009 Nov 16	C	3.2	3C120	3C120, 0532+075	32.0
All	C	8.4	43.8
All	D	8.4	31.9
All	Multi-configuration	20.0	52.3

3.4 Arcturus and Aldebaran

Currently the most detailed spatial information about the atmospheres of K and early M evolved stars is obtained from eclipsing binaries such as the ζ Aurigae and symbiotic systems (e.g., Wright 1970; Baade *et al.* 1996; Eaton 2008; Crowley *et al.* 2008). Even though these systems offer us the best opportunity to obtain information on the dynamics and thermodynamics at various heights in the evolved star’s atmosphere, the very nature of the binary system may introduce further complexities. For example, the orbital separation is often within the wind acceleration region and one could expect flow perturbations to be present (e.g., Chapman 1981). In fact, using the old VLA, Harper *et al.* (2005) were able to confirm that the velocity structure of ζ Aurigae is not typical of single stars with similar spectral types, such as λ Velorum (Carpenter *et al.*, 1999). In order to avoid the assumed additional complexities of a companion, we have selected two single luminosity class III red giants: Arcturus (α Boo: K2 III) and Aldebaren (α Tau: K5 III). These nearby red giants have been extensively studied at other wavelengths and their stellar parameters, which are summarized in Table x, are accurately known. These stars are predicted to be point sources at all frequencies between 1 and 50 GHz in all VLA configurations so our radio observations measure their total flux density, F_ν . For example, our observations which are discussed in Section 3.6, were taken in B configuration providing a maximum angular resolution of $\sim 0.14''$ at Q band which is $\approx 7 R_\star$ for both stars. Moreover, both stars have existing semi-empirical 1-D chromospheric and wind models which we directly compare to our data.

Arcturus (α Boo: K2 III)

Arcturus (α Boo: K2 III) is the nearest ($d = 11.3$ pc) and brightest ($V = -0.04$ mag) noncoronal red giant and is probably the best example of a red giant that can be studied in detail with the VLA. It is the leader of a group of stars that share a similar V space velocity (the component of stellar motion relative to the LSR in the direction of rotation), age (≥ 10 Gyr), and metallicity ($[\text{Fe}/\text{H}] \sim -0.5$), known as the Arcturus moving group (Eggen, 1971). The group has traditionally been regarded as the remains of a dissolved open cluster (e.g., Eggen, 1971, 1996)

but it has also been suggested to be the debris of a metal-poor accreted satellite some billions of years ago (Navarro *et al.*, 2004). Recent analysis of chemical abundances are consistent with the former hypothesis but do not entirely rule out a merger one (Williams *et al.*, 2009). Arcturus is ascending the red giant branch and being a single star, its mass is relatively poorly constrained but is similar to that of the Sun ($0.8 \pm 0.2 M_{\odot}$ by Kallinger *et al.*, 2010). During the last decade there has been a large dispersion in the reported values of Arcturus' effective temperature (a nice graph summarizing this is presented in Griffin, 1996) but nowadays it is generally accepted to be about 4300 K (di Benedetto, 1993). A number of interferometric measurements of the limb-darkened angular diameter of the star are available in the literature with most values agreeing within their uncertainties. The weighted mean value of these values is $\theta_{\text{LD}} = 21.06 \pm 0.17$ mas (Ramírez & Allende Prieto, 2011) giving the star a radius of $25.4 \pm 0.3 R_{\odot}$.

Arcturus is an important target for high spatial and spectral resolution calibration. Thus when the Hipparcos catalogue flagged Arcturus as a two component object (Perryman *et al.*, 1997) it caused quite a stir in the community. However, the uncertainties in the Hipparcos data (Soderhjelm & Mignard, 1998) along with a non-detection in adaptive optics observations (Turner *et al.*, 1999) and sensitive interferometric techniques (Lacour *et al.*, 2008) suggest that Arcturus is single and can still be used as a calibrator. Nevertheless, Lacour *et al.* (2008) still do not rule out the possibility of a planetary companion of a few Jovian masses as suggested by Hatzes & Cochran (1993) and Brown (2007). Variations in the order of a few days period are seen in its radial velocity (Merline, 1999) as well as photometry (Retter *et al.*, 2003). The photometric amplitude oscillations can vary by up to a percent and may be the manifestation of convection such as large-scale granulation, or solar-like oscillations (Dziembowski *et al.*, 2001).

The first detailed model of the atmosphere of Arcturus was the 1D time-independent semi-empirical model of Ayres & Linsky (1975) which was based on diagnostics observable from the ground (i.e. Ca II *h* and *k* and the Ca II IR triplet) and early satellite observations of Mg II *h* and *k* from *Copernicus*. They were able to calculate temperature and mass column densities for the upper photosphere and chromosphere and estimated the temperature at the top of the chromosphere to be ~ 8000 K. They also found that $T_{\text{min}}/T_{\text{eff}} \sim 0.77$ which is similar to that

3.4 Arcturus and Aldebaran

of the Sun. The important IUE cool star survey by [Linsky & Haisch \(1979\)](#) placed Arcturus on the right of the dividing line. This meant that its atmosphere showed lines formed at temperatures no hotter than 10,000 – 20,000 K, suggestive of a chromosphere only. However, they also developed a hot coronal wind

Table 3.3: Basic Properties of α Boo and α Tau.

Property	α Boo	α Tau	Reference
HD Number	124897	29139	...
Spectral Type	K2 III	K5 III	1
App. Mag. (V)	-0.5	0.86v	1
ra (ICRS: ep=J2000)	14 ^h 15 ^m 39.672 ^s	04 ^h 35 ^m 55.239 ^s	3
dec (ICRS: ep=J2000)	+19 10 56.673	+16 30 33.489	3
pm-ra (mas yr ⁻¹)	-1093.39 ± 0.44	63.45 ± 0.84	3
pm-dec (mas yr ⁻¹)	-2000.06 ± 0.39	-188.94 ± 0.65	3
π (mas)	88.83 ± 0.54	48.94 ± 0.77	3
Distance (pc)	11.3±0.1	20.4±0.3	3
M (M_{\odot})	0.8±0.2	1.3±0.3	6, 4
θ_{LD} (mas)	21.06±0.17	20.58±0.03	5a, 5b
R (R_{\odot})	25.4±0.3	44.2±0.9	...
T_{eff} (K)	4294±30	3970±49	5
L (L_{\odot})	calc	calc	...
Log g	calc	calc	...
v_{rad} (km s ⁻¹)	+5.19 ± 0.04	+54.11 ± 0.04	9
v_{esc} (km s ⁻¹)	110	106	...
v_{∞} (km s ⁻¹)	35 – 40	30	7, 8
T_{wind} (K)	~10,000	~10,000	7, 8
\dot{M} (M_{\odot} yr ⁻¹)	2×10^{-10}	1.6×10^{-11}	7, 8
H (H_{\odot})	calc	calc	...
Fe/H	-0.5 ± 0.2	-0.15 ± 0.2	10
Rotational period (yr)	2.0 ± 0.2	1.8	11
Chromosphere Model	Drake (1985)	McMurry (1999)	
Wind Model	Drake (1985)	Robinson <i>et al.</i> (1998)	

References.- (1) [Perryman *et al.* \(1997\)](#); (2) [Gray *et al.* \(2006\)](#); (3) [van Leeuwen \(2007\)](#); (5a) [Ramírez & Allende Prieto \(2011\)](#) (5b) [Richichi & Roccatagliata \(2005\)](#); (5) [di Benedetto \(1993\)](#); (6) [Kallinger *et al.* \(2010\)](#); (7) [Drake \(1985\)](#); (8) [Robinson *et al.* \(1998\)](#) (9) [Massarotti *et al.* \(2008\)](#); (10) [Decin *et al.* \(2003\)](#); (11) [Gray *et al.* \(2006\)](#); (12) [Hatzes & Cochran \(1993\)](#)

model for the star and found it to be consistent with the absence of transition region material in the IUE data; that is, the high temperature transition region emission line fluxes could be below the detection limit. Drake (1985) developed a semi-empirical chromosphere and wind model for Arcturus based on the Mg II k emission line from IUE and showed that its wind is very extended and estimated a mass loss rate of $2 \times 10^{-10} M_{\odot} \text{ yr}^{-1}$. Evidence began to emerge that Arcturus actually falls into the class of late type stars known as hybrids when deeply exposed IUE echelle spectrograms showed the weak presence of the Si III] $\lambda 1892.0$ feature, indicating the existence of a small amount of plasma at temperatures as hot as 6×10^4 K. Its hybrid status was confirmed when C IV and N V (indicative of temperatures $\sim 1 \times 10^5$ K) were detected with the HST STIS and also with a 3σ X-ray detection made with the Chandra X-Ray Observatory (Ayres *et al.*, 2003). The important conclusion is that Arcturus has been able to sustain a modest level of magnetic activity. In fact, a magnetic field (albeit weak) has recently been detected on the star (Sennhauser & Berdyugina, 2011) along with a magnetic cycle with a period of ≥ 14 years (Brown *et al.*, 2008).

Aldebaran (α Tau: K5 III)

At a distance of 20.4 pc, Aldebaran (α Tau: K5 III) is a nearby red giant and is one of the most easily recognizable stars from the northern and most of the southern hemisphere. Even though it is almost twice as far away as Arcturus, its large stellar radius ($R_{\star} = 44.2 \pm 0.9 R_{\odot}$) gives it a comparable angular diameter ($\theta_{\text{LD}} = 20.58 \pm 0.03$), and is therefore another good candidate for multi-frequency studies with the VLA. Its effective temperature ($T_{\text{eff}} = 3970 \pm 49$ K) is slightly lower than Arcturus', and also has a slightly higher mass ($M = 1.3 \pm 0.3$). Combining this mass and with a radius of xR_{\odot} results in a surface gravity of $\log g = x$ (in units of cm s^{-2}), x times lower than that of the Sun. The metallicity of Aldebaran is marginally subsolar with $[\text{Fe}/\text{H}] = -0.15 \pm 0.2$ (Decin *et al.*, 2003). Using high spectral resolution in the H, K, and L bands, Tsuji (2008) derived the carbon, nitrogen, and oxygen abundances in Aldebaran which suggests the mixing of the CN-cycled material in the first dredge-up. A 643 day period in the radial velocity for Aldebaran was reported by Hatzes & Cochran (1993) and Hatzes & Cochran (1998) find evidence to support the hypothesis that this

3.5 The Karl G. Jansky Very Large Array

variability comes from the reflex motion of the central star due to a planetary companion having a mass of $11M_{\text{jup}}$.

Aldebaran has been extensively studied at UV wavelengths. Early IUE observations placed the star well to the noncoronal side of the Linsky-Haisch dividing line (Linsky & Haisch, 1979). The first chromospheric model of the star was developed in the late 1970s (Kelch *et al.*, 1978) and was based on both optical (mainly Ca II H and K) and UV (Mg II *h* and *k*) emission line fluxes. Later, GHRS spectra revealed the presence of significant flux in the C IV resonance lines around 1550 Å (Carpenter & Robinson, 1996), indicating the presence of *hot* transition region plasma. In light of the new GHRS findings, a new model of the chromosphere and transition region of Aldebaran was developed, with temperatures reaching up to $T_e \sim 1 \times 10^5$ K. Modelling the GHRS optically thick Mg II and O I resonance lines (which show the most evidence for the stellar wind), Robinson *et al.* (1998) found evidence for the acceleration of a slow wind and derived a mass-loss rate of $1.6 \times 10^{-11} M_{\odot} \text{ yr}^{-1}$, and a terminal wind velocity of 30 km s^{-1} . Unexpectedly, FUSE spectra revealed the presence (albeit weak) of the coronal proxy O VI 1032 and 1038 Å emission lines (Dupree *et al.*, 2005) although Ayres *et al.* (2003) failed to detect any X-ray emission from the star.

3.5 The Karl G. Jansky Very Large Array

The Karl G. Jansky Very Large Array (VLA) is an aperture synthesis radio telescope located on the Plains of San Agustin, New Mexico, USA and is capable of producing radio images with a resolution comparable to that of optical telescopes. It is the product of a program to modernize the electronics of the old VLA which had been in operation since the late 1970's. One of the main upgrades to the VLA is the addition of the Wideband Interferometric Digital Architecture (WIDAR) correlator which allows the digital correlation of very wideband signals. WIDAR digitally filters and splits the data into sub-bands which are then separately cross-correlated and integrated before being stitched together again to yield the final wideband spectrum. The new WIDAR correlator and its superior

3.5 The Karl G. Jansky Very Large Array

Table 3.4: Improved Performance Parameters of the VLA.

Parameter	old VLA	VLA	Improvement Factor
Continuum sensitivity (1σ , 9 hr)	10 μ Jy	1 μ Jy	10
Bandwidth per polarization	0.1 GHz	8 GHz	80
Coarsest frequency resolution	50 MHz	2 MHz	25
Finest frequency resolution	381 Hz	0.12 Hz	3180
Channels at max. bandwidth	16	16,384	1024
Maximum number of channels	512	4,194,304	8192

bandwidth capability provides the VLA with greater sensitivity, allowing the detection of lower flux density sources than was previously possible with the old VLA. A comparison of the performance parameters of the VLA with those of the old VLA is shown in Table 3.5. The three major new observational abilities of the VLA are:

1. Complete frequency coverage between 1 and 50 GHz.
2. An increase in continuum sensitivity by an order of magnitude at some frequencies, by increasing the bandwidth to 8 GHz per polarization.
3. Process the large bandwidth with a minimum of 16,384 spectral channels per baseline.

Apart from the addition of more feeds at the center of the reflector, the structural design of the VLA has not changed during its recent upgrade. As before it consists of 27 fully steerable alt-azimuth antennas arranged along the arms of an upside-down ‘Y’ as shown in Figure 2.9. The array is reconfigurable and can vary its resolution by over a factor of ~ 50 through movement of its component antennas along twin railroad tracks. Four standard configurations of antennas along the arms of the array are possible whose scales vary by the ratios 1 : 3.28 : 10.8 : 35.5 from smallest to largest. These are called D, C, B, and A configurations, with A having the longest baselines (~ 36 km) giving the best angular resolution, but lacking short baselines needed for imaging extended structure. In each configuration, the distance of each antenna from the center of the ‘Y’ is equal to $m^{\ln 2}$ where m is the antenna location number, counting outwards from the center

3.5 The Karl G. Jansky Very Large Array

Table 3.5: Frequency coverage, primary beam, and angular resolution of the VLA.

	L	S	C	X	Ku	K	Ka	Q
ν (GHz)	1.5	3.0	6.0	10	15	22	33	45
λ (cm)	20	13	6.0	3.0	2.0	1.3	1.0	0.7
ν Range (GHz)	1-2	2-4	4-8	8-12	12-18	18-26.5	26.5-40	40-50
FOV: $\theta_{\text{HPBW}}^{\text{PB}}$ (')	30	15	7.5	4.5	3.0	2.0	1.4	1.0
A config: $\theta_{\text{HPBW}}^{\text{SB}}$ (")	1.3	0.65	0.33	0.20	0.13	0.089	0.059	0.043
B config: $\theta_{\text{HPBW}}^{\text{SB}}$ (")	4.3	2.1	1.0	0.6	0.42	0.28	0.19	0.14
C config: $\theta_{\text{HPBW}}^{\text{SB}}$ (")	14	7.0	3.5	2.1	1.4	0.95	0.63	0.47
D config: $\theta_{\text{HPBW}}^{\text{SB}}$ (")	46	23	12	7.2	4.6	3.1	2.1	1.5

of each arm. With this design, the m 'th station in any configuration coincides with the $2m$ 'th station in the next smaller configuration. This means that only 72 stations are needed to handle all four configurations. Additionally, there are 3 *hybrid* configurations called DnC, CnB, and BnA, which are well suited for sources with low declinations. In these configurations, the North arm antennas are deployed in the next larger configuration than the SE and SW arm antennas resulting in a more circular synthesized beam for these sources.

Each antenna is 25 m in diameter giving the array a total collecting area equivalent to a single dish of 130 m in diameter. Each antenna has an off-axis Cassegrain design with a rotatable sub-reflector at the prime focus of the main reflector and is supported by four feed legs. All feeds are located on a feed ring at the Cassegrain focus and the observing feed is changed by rotating the asymmetric sub-reflector about the main reflector axis so that the secondary focal point moves to the desired feed. The standard observing mode for all feeds is circular polarization. RF signals from each feed are sent via a waveguide to the antenna vortex room located directly underneath the main reflector where they are feed into low noise front ends. The vortex room is temperature controlled and also contains cryogenic cooling systems for the front end, portions of the LO, and IF equipment. IF signals from each antenna are sent by cable to a shielded room where the sampler and delay and multiplier racks are located. **Once the signals have been cross-correlated they are time averaged into visibility measurements.**

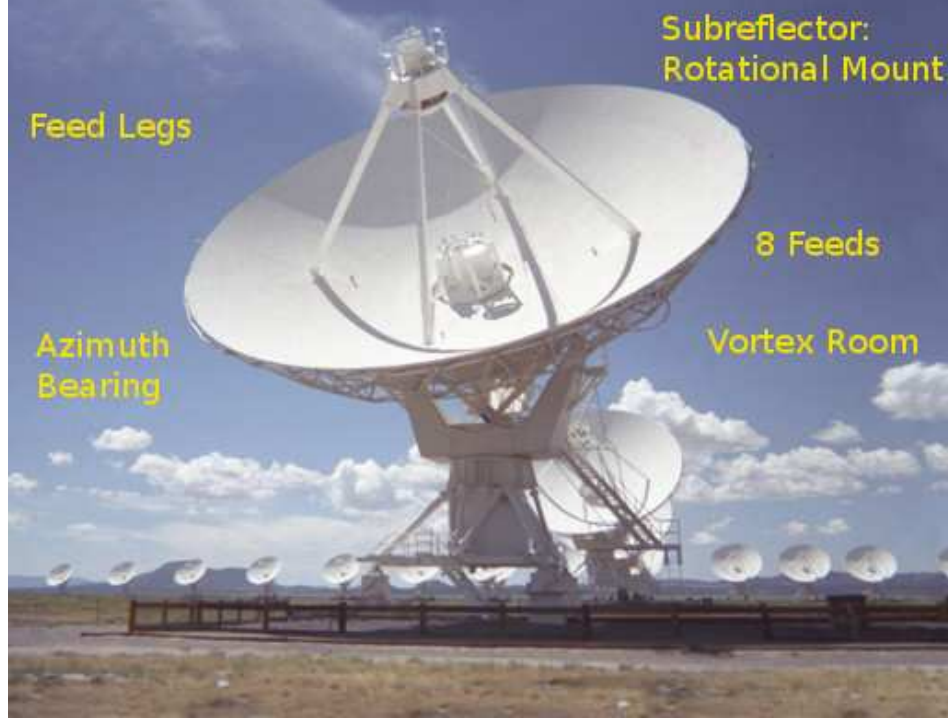


Figure 3.1: Main features of a VLA antenna. The sub-reflector is located at prime focus on a rotational mount is supported by four feed legs. The 8 feeds are located in a ring at the secondary focus. The feeds send the RF signal to the front end located in the vortex room directly beneath the main reflector.

All VLA antennas are outfitted with eight receivers providing continuous frequency coverage between 1 and 50 GHz. As shown in Table x, the frequency ranges of 1-2 GHz, 2-4 GHz, 4-8 GHz, 8-12 GHz, 12-18 GHz, 18-26.5 GHz, 26.5-40 GHz, and 40-50 GHz, are commonly referred to as L, S, C, X, Ku, K, Ka, and Q bands, respectively. Additionally, the VLA is currently being outfitted with even lower frequency receivers, P-band (230-470 MHz) and 4-band (54-86 MHz). The VLA's angular resolution is set by the maximum baseline B_{\max} and frequency of observation. This means that structures smaller than the diffraction limit ($\theta_{\text{HPBW}}^{\text{SB}} \sim \lambda/B_{\max}$) will be smoothed to the resolution of the array. Table x summarizes the maximum resolution for each of the four main configurations at each wavelength. The resolution is defined here as the HPBW of the synthesized beam, using uniform weighting, over a full 12 hour synthesis observation of a source which passes near the zenith. For completeness, we also give the field of

view (FOV) at each observing frequency in Table x, defined as the HPBW of the primary beam, which for the VLA antennas can be approximated using the formula: $\theta_{\text{HPBW}}^{\text{PB}}(^{\circ}) = 45/\nu_{\text{GHz}}$.

3.6 VLA Observations of Arcturus and Aldebaran

The Open Shared Risk Observing (OSRO) program at the VLA existed during its commissioning phase to provide observers with early access to a number of VLA correlator capabilities and observing modes. This represented a considerable improvement over the capabilities of the old VLA correlator as observers were provided with increased bandwidth capability at existing VLA bands, increased spectral resolution capabilities, and access to new spectral bands. In September 2010 our proposal (PI: G. M. Harper, Program ID: 10C-105) to observe two archetypical red giants at multiple frequencies was allocated the requested 15.5 hours of observing time with the VLA as part of NRAO's OSRO Science Program 2010C. A number of observing scripts called scheduling blocks (SBs) were prepared during December 2010 and their duration were kept to ≤ 2.5 hours to increase their likelihood of being scheduled. The VLA now uses dynamic scheduling for deciding which SBs are executed at any time. It takes into account many factors like the scheduling priority assigned by the time allocation committee, weather constraints, and SB duration. Dynamic scheduling means that the observer does not know when their observations will occur but in general, the chances of observations being scheduled are increased if the duration of the SB is kept short.

Table 3.6: VLA Observations of α Boo and α Tau obtained in February 2011 and July 2012.

Star	Date	Band	ν (GHz)	λ (cm)	Time on Star (hr)	Restoring Beam ($'' \times ''$)	Bandwidth (GHz)	Number of Antennas	Phase Calibrator
α Boo	2011 Feb 22	Q	43.3	0.7	0.3	0.19×0.15	0.256	22	J1357+1919
	2011 Feb 22	Ka	33.6	0.9	0.2	0.25×0.20	0.256	23	J1357+1919
	2011 Feb 22	K	22.5	1.3	0.4	0.35×0.28	0.256	24	J1357+1919
	2011 Feb 11	X	8.5	3.5	0.3	1.14×0.70	0.256	18	J1415+1320
	2011 Feb 11	C	5.0	6.0	0.5	2.02×1.30	0.256	21	J1415+1320
	2011 Feb 13	S	3.1	9.5	1.8	2.57×2.08	0.256	12	J1415+1320
	2012 Jul 19	S	3.0	10.0	0.7	2.82×2.30	2.0	23	J1415+1320
	2012 Jul 20	L	1.5	20.0	1.6	4.46×3.94	1.0	23	J1415+1320
α Tau	2011 Feb 11	Q	43.3	0.7	0.3	0.18×0.16	0.256	22	J0431+1731
	2011 Feb 11	Ka	33.6	0.9	0.2	0.22×0.20	0.256	19	J0449+1121
	2011 Feb 11	K	22.5	1.3	0.4	0.35×0.31	0.256	21	J0449+1121
	2011 Feb 13	X	8.5	3.5	0.5	0.85×0.78	0.256	25	J0449+1121
	2011 Feb 13	C	5.0	6.0	1.2	1.48×1.32	0.256	21	J0449+1121
	2011 Feb 12	S	3.1	9.5	1.8	2.74×2.02	0.256	11	J0431+2037

3.6 VLA Observations of Arcturus and Aldebaran

Our main set of observations took place in February 2011 while the VLA was in B-configuration. All observations were taken in continuum mode and the correlator was set up with two 128 MHz sub-bands centered on the frequencies listed in Table x. Each sub-band had sixty-four channels of width 2 MHz and four polarization products (RR, LL, RL, LR). We obtained all our requested observations of α Tau in just two days between the 11th and 13th of February 2011 which consisted of Q, Ka, K, X, C, and S band observations of the star. We did not request L band (i.e. 1.5 GHz) observations of α Tau as it was believed that the star would be too faint to be observable at this frequency. There was also insufficient Ku band receivers available at the time to carry out observations at 15 GHz. We obtained Q, Ka, K, X, C, and S band observations of α Boo in eleven days between the 11th and 22nd of February 2011. We also had prepared a 2.5 hour SB for α Boo at L-band but this SB was never executed.

For this reason we applied for (and were awarded) 3 additional hours of directors discretionary time (DDT) in early 2012 (PI: E. O’Gorman, Program ID: 12A-472) to observe α Boo at S and L band. We decided to include a short observation at S band even though we already had an observation at this band to make sure that the stars flux density had not significantly changed over that period and so any possible L band detection could be included in the analysis of the main set of data from the previous year. Our DDT observations took place in July 2012 when the VLA was again in B-configuration and some of these details are given in Table x. The capabilities of the VLA had greatly increased in the ~ 1.5 years since the main set of observations and we now could utilize the full 1 and 2 GHz of bandwidth at L and S band, respectively. The 1-2 GHz and 2-4 GHz frequency ranges were both divided into 16 sub-bands, each with sixty-four channels. The channel width was 2 and 1 MHz for S and L-band, respectively, and each sub-band had four polarization products (RR, LL, RL, LR).

In radio interferometry, baseline-dependent additive errors in the visibilities can occasionally lead to artifacts occurring at phase center of the final image. Such errors may be caused by unflagged low level interference picked up by some antennas baselines. An example of this is demonstrated in Figure x in which two radio images of Betelgeuse at 15 GHz are shown (A. Brown, priv. comm.). The left panel was taken on 2nd February **2002** and shows a 30σ detection of

3.6 VLA Observations of Arcturus and Aldebaran

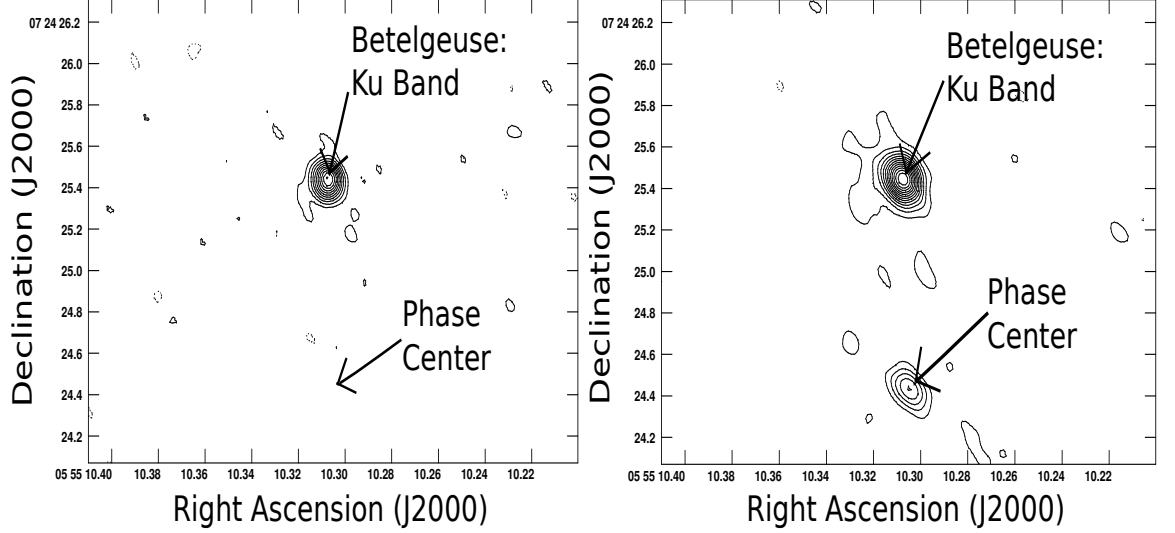


Figure 3.2: An example to highlight the importance of offsetting the source from phase center. *Left:* Old VLA image of Betelgeuse at 15 GHz taken on showing no source at the phase center of the image. Contour levels at $\sigma(-6, -3, 3, \dots, 30)$ where $\sigma = 84 \mu\text{Jy}$. *Right:* Two months later Betelgeuse was again image at 15 GHz but now shows a strong artifact at phase center. Contour levels at $\sigma(-6, -3, 3, \dots, 45)$ where $\sigma = 90 \mu\text{Jy}$ (A. Brown, priv. comm.).

Betelgeuse with low level background noise. The right panel which was taken two months later on 2nd April **2002** again shows a strong 45σ detection of the star but also now shows a 15σ artifact at phase center. If the target had been observed at phase center in this case, then this artifact would lead to an incorrect flux density measurement for the star. For our VLA observations, both α Boo and α Tau were slightly offset from the phase-center by ~ 5 synthesized beam widths in order to avoid source contamination by any phase center artifacts and to avoid spurious detections.

The main problem at low VLA frequencies (L and S bands) is disturbances in the ionosphere caused by solar activity. At L-band, solar flares can be as strong as 1×10^6 Jy and are a major source of interference, with their effects sometimes being impossible to remove from the data. To avoid such problems the S and L band SBs were scheduled for night time observing only. The low to intermediate frequency observations (L - X bands) were composed of repeatedly interleaved observations of the target and a nearby phase calibrator with cycle times of 12 minutes; 10 minutes on the target and 2 minutes on the phase calibrator. For α

3.6 VLA Observations of Arcturus and Aldebaran

Boo, the point source J1415+1320 which is located 6° away was used as the phase calibrator at these frequencies. For α Tau, the point source J0449+1121 located 6° away was used at C and X band, while the brighter J0431+2037 located 4° away was used at S band due to it being unresolved at this frequency (but is resolved at C and X band). The primary calibration sources 3C286 and 3C138 were observed at the end of all low and intermediate frequency SBs and were used to measure the bandpass and set the absolute flux for α Boo and α Tau, respectively. The top panel in Figure x shows a plot of elevation against time for all the sources observed in the SB of the C and X band observations of α Tau. In this SB, observations of α Tau at X band were interspersed between C band observations throughout the track to obtain a good spread in $u - v$ coverage.

At high VLA frequencies (i.e. K, Ka, and Q band) the troposphere can cause major phase variations to incoming radio waves. To reduce this problem, the old VLA used a technique called *fast switching* which reduced the setup overhead and slewing compared to traditional iterating between source and calibrator scans. This overhead is sufficiently reduced with the new VLA and no special fast switching mode is necessary. Instead regular but short duration source-calibrator loops are implemented. As a result, the calibration overheads for high frequency observing are typically considerably larger than for lower frequency observations. For both stars, the total cycle times for the Q, Ka, and K-band observations were 160, 230, and 290 s, respectively. These high frequency observations were combined into a single 2 hour SB for each star and commenced with X-band reference pointing with solutions being applied on-line. As mentioned in Section x, the blind pointing errors of the VLA antennas can occasionally be as large as the HPBW of the primary beam at high frequencies. Thankfully, the pointing can be calibrated for using a technique known as *reference pointing* whereby a nearby known calibrator is observed in interferometer pointing mode every hour or so. The measured local pointing corrections are then be applied to subsequent target observations. Reference pointing can reduce the rms pointing errors to as little as $2''$ if the reference source is within 10° of the target source. After X-band pointing the target source was observed at Q-band to ensure the best pointing solutions were used as shown in the lower panel of Figure x for α Tau.

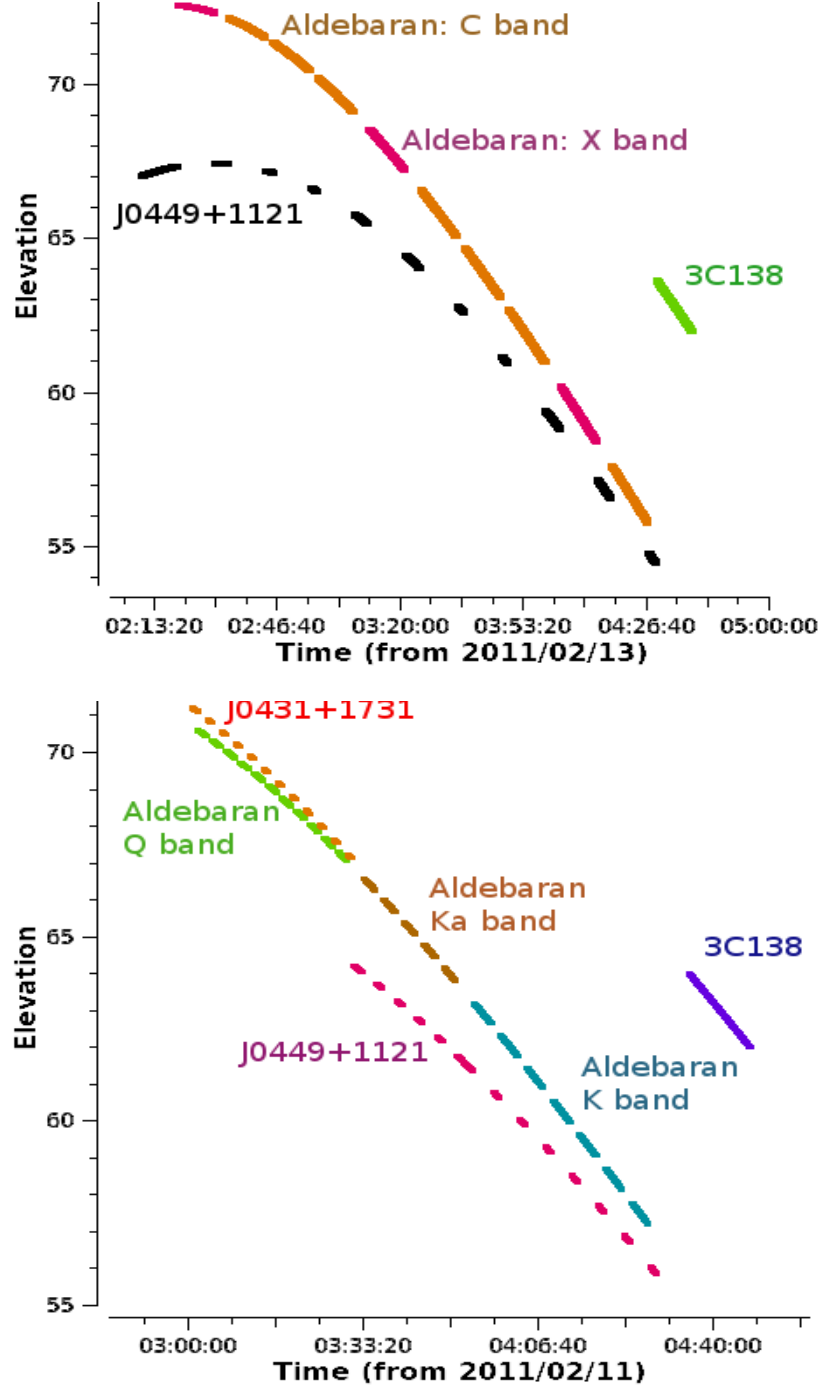


Figure 3.3: Overview of a low and high frequency VLA SB for α Tau. *Top Panel:* The low frequency observations consisted of interleaved observations of the target and a nearby phase calibrator with cycle times of 12 minutes. The X band observations were interspersed between C band observations to obtain a good spread in $u-v$ coverage. *Bottom Panel:* The high frequency observations had short cycle times to compensate for tropospheric effects. Q band observations were taken first to ensure the best pointing solutions were applied to them.



A Nice Appendix

This is where the appendix would go...

References

- AYRES, T.R. & LINSKY, J.L. (1975). Stellar model chromospheres. III - Arcturus /K2 III/. *Astrophysical Journal*, **200**, 660–674. (Cited on page 32.)
- AYRES, T.R., BROWN, A. & HARPER, G.M. (2003). Buried Alive in the Coronal Graveyard. *Astrophysical Journal*, **598**, 610–625. (Cited on pages 34 and 35.)
- BAADE, R., KIRSCH, T., REIMERS, D., TOUSSAINT, F., BENNETT, P.D., BROWN, A. & HARPER, G.M. (1996). The Wind Outflow of zeta Aurigae: A Model Revision Using Hubble Space Telescope Spectra. *Astrophysical Journal*, **466**, 979. (Cited on page 31.)
- BROWN, K.I.T. (2007). Long-Term Spectroscopic and Precise Radial Velocity Monitoring of Arcturus. *Publications of the Astronomical Society of the Pacific*, **119**, 237–237. (Cited on page 32.)
- BROWN, K.I.T., GRAY, D.F. & BALIUNAS, S.L. (2008). Long-Term Spectroscopic Monitoring of Arcturus. *Astrophysical Journal*, **679**, 1531–1540. (Cited on page 34.)
- CARPENTER, K.G. & ROBINSON, R.D. (1996). HST Studies of Carbon and K-M Giant/Supergiant Stars. In P. Benvenuti, F.D. Macchetto & E.J. Schreier, eds., *Science with the Hubble Space Telescope - II*, 418. (Cited on page 35.)
- CARPENTER, K.G., ROBINSON, R.D., HARPER, G.M., BENNETT, P.D., BROWN, A. & MULLAN, D.J. (1999). GHRS Observations of Cool, Low-Gravity Stars. V. The Outer Atmosphere and Wind of the Nearby K Supergiant lambda Velorum. *Astrophysical Journal*, **521**, 382–406. (Cited on page 31.)
- CHAPMAN, R.D. (1981). The 1979-1980 eclipse of Zeta Aurigae. I - The circumstellar envelope. *Astrophysical Journal*, **248**, 1043–1052. (Cited on page 31.)
- CROWLEY, C., ESPEY, B.R. & MCCANDLISS, S.R. (2008). EG And: Far Ultraviolet Spectroscopic Explorer and Hubble Space Telescope STIS Monitoring of an Eclipsing Symbiotic Binary. *Astrophysical Journal*, **675**, 711–722. (Cited on page 31.)
- DECIN, L., VANDENBUSSCHE, B., WAELEKENS, C., DECIN, G., ERIKSSON, K., GUSTAFSSON, B., PLEZ, B. & SAUVAL, A.J. (2003). ISO-SWS calibration and the accurate modelling of cool-star atmospheres. IV. G9 to M2 stars. *Astronomy & Astrophysics*, **400**, 709–727. (Cited on pages 33 and 34.)
- DI BENEDETTO, G.P. (1993). Empirical effective temperatures and angular diameters of stars cooler than the sun. *Astronomy & Astrophysics*, **270**, 315–334. (Cited on pages 32 and 33.)

REFERENCES

- DRAKE, S.A. (1985). Modeling lines formed in the expanding chromospheres of red giants. In J.E. Beckman & L. Crivellari, eds., *Progress in stellar spectral line formation theory; Proceedings of the Advanced Research Workshop, Trieste, Italy, September 4-7, 1984 (A86-37976 17-90)*. Dordrecht, D. Reidel Publishing Co., 1985, p. 351-357., 351–357. (Cited on pages 33 and 34.)
- DUPREE, A.K., LOBEL, A., YOUNG, P.R., AKE, T.B., LINSKY, J.L. & REDFIELD, S. (2005). A Far-Ultraviolet Spectroscopic Survey of Luminous Cool Stars. *Astrophysical Journal*, **622**, 629–652. (Not cited.)
- DZIEMBOWSKI, W.A., GOUGH, D.O., HOUDEK, G. & SIENKIEWICZ, R. (2001). Oscillations of α UMa and other red giants. *Monthly Notices of the Royal Astronomical Society*, **328**, 601–610. (Cited on page 32.)
- EATON, J.A. (2008). A Model for the Chromosphere/Wind of 31 Cygni and Its Implications for Single Stars. *Astronomical Journal*, **136**, 1964–1979. (Cited on page 31.)
- EGGEN, O.J. (1971). The Arcturus Group. *Publications of the Astronomical Society of the Pacific*, **83**, 271. (Cited on page 31.)
- EGGEN, O.J. (1996). Star Streams and Galactic Structure. *Astronomical Journal*, **112**, 1595. (Cited on page 31.)
- GRAY, R.O., CORBALLY, C.J., GARRISON, R.F., MCFADDEN, M.T., BUBAR, E.J., MCGAHEE, C.E., O'DONOGHUE, A.A. & KNOX, E.R. (2006). Contributions to the Nearby Stars (NStars) Project: Spectroscopy of Stars Earlier than M0 within 40 pc-The Southern Sample. *Astronomical Journal*, **132**, 161–170. (Cited on page 33.)
- GRIFFIN, R.E.M. (1996). Arcturus and human evolution. *The Observatory*, **116**, 404–405. (Cited on page 32.)
- HARPER, G.M., BROWN, A., BENNETT, P.D., BAADE, R., WALDER, R. & HUMMEL, C.A. (2005). VLA Observations of ζ Aurigae: Confirmation of the Slow Acceleration Wind Density Structure. *Astronomical Journal*, **129**, 1018–1034. (Cited on page 31.)
- HATZES, A.P. & COCHRAN, W.D. (1993). Long-period radial velocity variations in three K giants. *Astrophysical Journal*, **413**, 339–348. (Cited on pages 32, 33 and 34.)
- HATZES, A.P. & COCHRAN, W.D. (1998). On the nature of the radial velocity variability of Aldebaran - A search for spectral line bisector variations. *Monthly Notices of the Royal Astronomical Society*, **293**, 469. (Cited on page 34.)
- HÖGBOM, J.A. (1974). Aperture Synthesis with a Non-Regular Distribution of Interferometer Baselines. *Astronomy & Astrophysics Supplemental*, **15**, 417. (Cited on page 26.)
- JACKSON, N. (2008). Principles of Interferometry. In F. Bacciotti, L. Testi & E. Whelan, eds., *Jets from Young Stars II*, vol. 742 of *Lecture Notes in Physics*, Berlin Springer Verlag, 193. (Cited on pages 14 and 16.)
- KALLINGER, T., WEISS, W.W., BARBAN, C., BAUDIN, F., CAMERON, C., CARRIER, F., DE RIDDER, J., GOUPIL, M.J., GRUBERBAUER, M., HATZES, A., HEKKER, S., SAMADI, R. & DELEUIL, M. (2010). Oscillating red giants in the CoRoT exofield: asteroseismic mass and radius determination. *Astronomy & Astrophysics*, **509**, A77. (Cited on pages 32 and 33.)

REFERENCES

- KELCH, W.L., CHANG, S.H., FURENLID, I., LINSKY, J.L., BASRI, G.S., CHIU, H.Y. & MARAN, S.P. (1978). Stellar model chromospheres. VII - Capella /G5 III +/, Pollux /K0 III/, and Aldebaran /K5 III/. *Astrophysical Journal*, **220**, 962–979. (Cited on page 35.)
- KRAUS, J.D., TIURI, M., RAISANEN, A.V. & CARR, T.D. (1986). *Radio astronomy receivers*. (Cited on page 5.)
- LACOUR, S., MEIMON, S., THIÉBAUT, E., PERRIN, G., VERHOELST, T., PEDRETTI, E., SCHULLER, P.A., MUGNIER, L., MONNIER, J., BERGER, J.P., HAUBOIS, X., PONCELET, A., LE BESNERAIS, G., ERIKSSON, K., MILLAN-GABET, R., RAGLAND, S., LACASSE, M. & TRAUB, W. (2008). The limb-darkened Arcturus: imaging with the IOTA/IONIC interferometer. *Astronomy & Astrophysics*, **485**, 561–570. (Cited on page 32.)
- LINSKY, J.L. & HAISCH, B.M. (1979). Outer atmospheres of cool stars. I - The sharp division into solar-type and non-solar-type stars. *Astrophysical Journal Letters*, **229**, L27–L32. (Cited on pages 33 and 35.)
- MASSAROTTI, A., LATHAM, D.W., STEFANIK, R.P. & FOGEL, J. (2008). Rotational and Radial Velocities for a Sample of 761 HIPPARCOS Giants and the Role of Binarity. *Astronomical Journal*, **135**, 209–231. (Cited on page 33.)
- MCMURRY, A.D. (1999). The outer atmosphere of Tau - I. A new chromospheric model. *Monthly Notices of the Royal Astronomical Society*, **302**, 37–47. (Cited on page 33.)
- MERLINE, W.J. (1999). Precise Velocity Observation of K-Giants: Evidence for Solar-Like Oscillations in Arcturus. In J.B. Hearnshaw & C.D. Scarfe, eds., *IAU Colloq. 170: Precise Stellar Radial Velocities*, vol. 185 of *Astronomical Society of the Pacific Conference Series*, 187. (Cited on page 32.)
- MICHELSON, A.A. (1890). . *Phil. Mag.*, **30**, 1–21. (Cited on page 20.)
- NAVARRO, J.F., HELMI, A. & FREEMAN, K.C. (2004). The Extragalactic Origin of the Arcturus Group. *Astrophysical Journal Letters*, **601**, L43–L46. (Cited on page 32.)
- PERRYMAN, M.A.C., LINDEGREN, L., KOVALEVSKY, J., HOEG, E., BASTIAN, U., BERNACCA, P.L., CRÉZÉ, M., DONATI, F., GRENON, M., GREWING, M., VAN LEEUWEN, F., VAN DER MAREL, H., MIGNARD, F., MURRAY, C.A., LE POOLE, R.S., SCHRIJVER, H., TURON, C., ARENOU, F., FROESCHLÉ, M. & PETERSEN, C.S. (1997). The HIPPARCOS Catalogue. *Astronomy & Astrophysics*, **323**, L49–L52. (Cited on pages 32 and 33.)
- PROTHERO, D. & BUELL, C. (2007). *Evolution: what the fossils say and why it matters*. Columbia University Press. (Cited on page 1.)
- RAMÍREZ, I. & ALLENDE PRIETO, C. (2011). Fundamental Parameters and Chemical Composition of Arcturus. *Astrophysical Journal*, **743**, 135. (Cited on pages 32 and 33.)
- RETTET, A., BEDDING, T.R., BUZASI, D.L., KJELDSSEN, H. & KISS, L.L. (2003). Oscillations in Arcturus from WIRE Photometry. *Astrophysical Journal Letters*, **591**, L151–L154. (Cited on page 32.)
- RICHICHI, A. & ROCCATAGLIATA, V. (2005). Aldebaran’s angular diameter: How well do we know it? *Astronomy & Astrophysics*, **433**, 305–312. (Cited on page 33.)

REFERENCES

- ROBINSON, R.D., CARPENTER, K.G. & BROWN, A. (1998). Goddard High-Resolution Spectrograph Observations of Cool Low-Gravity Stars. IV. A Comparison of the K5 III Stars alpha Tauri and gamma Draconis. *Astrophysical Journal*, **503**, 396. (Cited on pages [33](#) and [35](#).)
- SAGAN, C. (1997). *The Demon-Haunted World: Science as a Candle in the Dark*. Ballantine Books. (Cited on page [1](#).)
- SENNHAUSER, C. & BERDYUGINA, S.V. (2011). First detection of a weak magnetic field on the giant Arcturus: remnants of a solar dynamo? *Astronomy & Astrophysics*, **529**, A100. (Cited on page [34](#).)
- SODERHJELM, S. & MIGNARD, F. (1998). Arcturus as a double star. *The Observatory*, **118**, 365–366. (Cited on page [32](#).)
- TAYLOR, G.B., CARILLI, C.L. & PERLEY, R.A., eds. (1999). *Synthesis Imaging in Radio Astronomy II*, vol. 180 of *Astronomical Society of the Pacific Conference Series*. (Cited on pages [9](#) and [10](#).)
- TSUJI, T. (2008). Cool luminous stars: the hybrid nature of their infrared spectra. *Astronomy & Astrophysics*, **489**, 1271–1289. (Cited on page [34](#).)
- TURNER, N.H., TEN BRUMMELAAR, T.A. & MASON, B.D. (1999). Adaptive Optics Observations of Arcturus using the Mount Wilson 100 Inch Telescope. *Publications of the Astronomical Society of the Pacific*, **111**, 556–558. (Cited on page [32](#).)
- VAN LEEUWEN, F. (2007). Validation of the new Hipparcos reduction. *Astronomy & Astrophysics*, **474**, 653–664. (Cited on page [33](#).)
- WILLIAMS, M.E.K., FREEMAN, K.C., HELMI, A. & RAVE COLLABORATION (2009). The Arcturus Moving Group: Its Place in the Galaxy. In J. Andersen, Nordströara, B. m & J. Bland-Hawthorn, eds., *IAU Symposium*, vol. 254 of *IAU Symposium*, 139–144. (Cited on page [32](#).)
- WRIGHT, K.O. (1970). The Zeta Aurigae stars. *Vistas in Astronomy*, **12**, 147–182. (Cited on page [31](#).)